The Effects of Dynamical Diffraction on the Measurement of Gravitationally Induced Quantum Phase Shifts by Neutron Interferometry

K. C. LITTRELL,[a] B. E. ALLMAN,[b] O. I. MOTRUNICH[c] AND S. A. WERNER[d]*

[a]*Intense Pulsed Neutron Source, Argonne National Laboratory, Argonne, IL 60439, USA,* [b]*School of Physics, University of Melbourne, Parkville, Victoria 3052, Australia,* [c]*Physics Department, Princeton University, Princeton, NJ 08540, USA, and* [d]*Physics Department and Research Reactor Center, University of Missouri-Columbia, Columbia, MO 65211, USA. E-mail: werner@nopt.physics.missouri.edu*

Abstract

The proper analysis of experiments to measure the quantum-mechanical phase shift due to potential gradients such as gravity across a perfect-silicon-crystal Mach–Zehnder interferometer for neutrons is complicated by the highly dispersive nature of the dynamical diffraction process describing the propagation of neutrons through a perfect crystal. Through dynamical diffraction, a coherent monochromatic incident beam of neutrons that does not exactly satisfy the Bragg condition is split into two currents within each crystal so that there are 16 possible coherent interfering trajectories by which the neutron can traverse the interferometer. In this work, previous calculations of the effects of dynamical diffraction on gravitationally induced phase-shift measurements are extended to include effects in all exit beams and internal effects within the subbeams for both symmetric and skew-symmetric interferometers. For the interferometers used in a recent experiment in which the gravitationally induced phase shift of the neutron is measured with a statistical uncertainty of the order of 1 part in 1000, it is found that these effects predict an increase of a few percent in the magnitude of the phase shift. Additionally, some consequences on the phase and contrast of restricting the beams within and after the interferometer are discussed. Agreement of this theory with experiment and the general applicability of the model is discussed.

1. Introduction

The influence of gravity on the quantum-mechanical phase of the neutron de Broglie wave in a neutron interferometer was first observed by Colella *et al.* (1975) and then more accurately by Staudenmann *et al.* (1980), beginning a series of experiments of increasing sophistication (Werner *et al.*, 1986, 1988; Werner, 1994; Jacobson, 1997; Littrell *et al.*, 1996, 1997). The results of these experiments, collectively known as COW experiments, necessarily depend on both Planck's constant $\hbar$ and Newton's universal gravitational constant G. This dependence allows the principle of equivalence to be studied in the quantum limit.

The validity of the classical principle of equivalence has been verified to a very high precision (Roll *et al.*, 1967). Similarly, it has been demonstrated (Koester, 1975) that the probability density of a neutron in the Earth's gravitational field follows the same parabolic trajectory as a classical point particle with the same inertial mass to within an uncertainty of 3 parts in 10 000. The most recent precise measurements of the COW type (Werner *et al.*, 1988; Littrell *et al.*, 1997) have shown disturbing discrepancies on the order of 1% between theory (including all known corrections) and experiment. Statistical errors and estimated and measured uncertainties in the experimental parameters are on the order of 1 part in 1000.

The experimental arrangement for a measurement of the phase shift of a neutron due to the Earth's gravitational field is shown in Fig. 1. A nearly monochromatic collimated beam of neutrons is incident upon a neutron
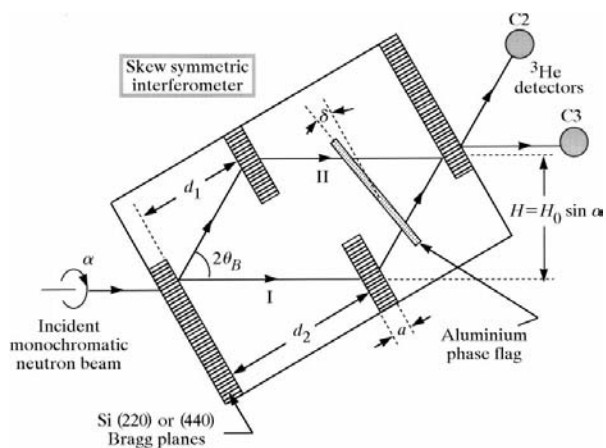

Fig. 1. A schematic diagram of the experimental arrangement. One beam of the interferometer is raised above the other by tilting the interferometer an angle α about the incident beam. An additional phase shift due to the interaction of neutrons with matter can be introduced by rotating an aluminium phase shifter extending across both subbeams through an angle δ.

interferometer constructed out of a single perfect crystal of silicon. The crystal lattice of the silicon acts as a three-dimensional diffraction grating for neutrons, allowing the various blades of the interferometer to act as mirrors or beam splitters due to Bragg diffraction. A perfect crystal is used to ensure that the lattice planes of the various blades are perfectly aligned. The first blade of the interferometer splits the neutron beam into two components that are redirected by the intermediate blades to recombine in the final blade. The interferometers used in these experiments, first developed for X-rays by Bonse & Hart (1965) and demonstrated to work for thermal neutrons by Rauch et al. (1974), are analogous in geometry to Mach–Zehnder interferometers for light. The difference in optical path length and therefore the phase accumulated by a neutron along one path relative to the other can be modified by varying the potential energy of the neutron along either of the two spatially separated beam paths. These differences in accumulated phase are measured as the exchange of intensity back and forth between the two ^{3}He proportional detectors labeled C2 and C3 in Fig. 1.

It is possible to produce phase shifts in these experiments either by changing the neutron–nuclear optical potential or the gravitational potential energy of the neutron along one path relative to the other. The phase shift due to the neutron–nuclear optical potential is adjusted using a 1 mm thick aluminium phase flag. The phase flag is placed across both beams and rotated through the angle labeled δ in Fig. 1 about an axis perpendicular to the scattering plane of the interferometer, varying the difference in optical path length that the two beams must travel in aluminium. A gravitational phase shift is produced by tilting the entire assembly consisting of the interferometer, detectors and phase flag about the incident beam of neutrons through the angle labeled α in Fig. 1 so that the horizontal portions of the two beam paths labeled I and II in Fig. 1 are at different heights and thus different gravitational potentials.

The dynamical theory of diffraction for neutrons predicts that neutrons that nearly, but not exactly, satisfy the Bragg condition follow several trajectories through the interferometer. Since these paths form multiple interacting interferometers, the interference pattern observed as the interferometer is tilted in a gravitational field differs greatly from that expected from assuming the simple two-path Mach–Zehnder interferometer geometry that describes the case when the Bragg condition is exactly satisfied. These effects must be understood in order to properly interpret the results of a gravitational phase-shift measurement. In this paper, we extend previous calculations (Horne, 1986; Werner et al., 1988) of the effects of dynamical diffraction on the intensity measured in the C3 (or O-beam) detector using symmetric interferometers to include effects in the C2

(or G-beam) and skew-symmetric interferometers. We also analyze interference effects internal to each of the two beams independent of the other and the resulting single-beam gravity-induced phase shifts observable in the C1 beam and the C4 beam. Finally, we discuss interference effects observed in the C2 and C3 beam detectors when one beam of the interferometer is blocked.

Our theoretical predictions for various diffraction and interference effects are compared with data obtained with the two interferometers used in a recently completed experiment (Littrell et al., 1997) in which we used neutrons to characterize both the phase shifts due to bending of the interferometer and due to gravity acting on the neutron wavefunction as a function of the tilt angle α. The device shown in Fig. 2 is a skew-symmetric interferometer with blade separations $d_1 = 16.172\,(3)$ mm and $d_2 = 49.449\,(3)$ mm and blade thickness $a = 2.621\,(3)$ mm. The other interferometer, shown in Fig. 3, is a symmetric interferometer similar in geometry to the ones used in previous COW experiments but larger in size and therefore more sensitive. It has a separation between blades $d_1 = d_2 = 50.404\,(3)$ mm and a blade thickness of 3.077 (3) mm. The interferometers were machined from high-purity semiconductor-quality nearly perfect single-crystal silicon ingots using a combination of 200 and 400 grit diamond wheels and subsequently etched in the standard silicon etchant mixture of 18% hydrofluoric acid, 52% nitric acid and 25% glacial acetic acid by volume to reduce the strains induced by machining by removing approximately 70 mm of material from all surfaces.

The incident beam was defined by a circular aperture 7 mm in diameter placed perpendicular to the incident
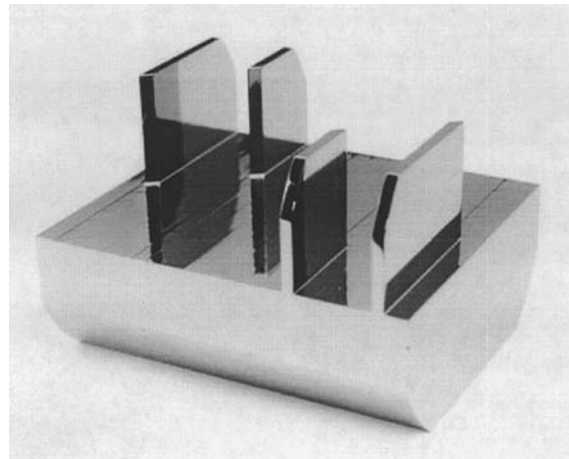

Fig. 2. A photograph of the skew-symmetric interferometer used in this experiment. The dimensions (defined in Fig. 1) of the interferometer are $d_1 = 16.172$ mm, $d_2 = 49.449$ mm and $a = 2.621$ mm. This interferometer was machined in the physics shop at the University of Missouri–Columbia.

beam 5 cm from the splitter blade of the interferometer for measurements with the skew-symmetric interferometer and by one 10 mm in diameter for those measurements using the symmetric interferometer.

2. Theoretical background

The most convenient reference frame for calculation of the phase shift due to gravity is the frame of the interferometer at rest on the surface of the Earth. Since the Lagrangian $\mathcal{L}$ of the neutron in the rotating frame of the Earth is time independent, the phase shift in the interferometer can be calculated from the path integral

$$\Delta\Phi = (1/\hbar)\left[\int_{\text{path II}} \mathbf{p} \cdot \mathbf{dl} - \int_{\text{path I}} \mathbf{p} \cdot \mathbf{dl}\right], \qquad (1)$$

where

$$\mathbf{p} = \partial\mathcal{L}/\partial\mathbf{v} = m_i\mathbf{v} + m_i\omega \times \mathbf{x} \qquad (2)$$

is the canonical momentum of the neutron in this frame. In this expression, $\mathbf{v}$ is the velocity of the neutron in the laboratory frame as obtained from the classical equations of motion, $\mathbf{x}$ is its position vector relative to the interferometer, m_i is its inertial mass, and ω is the Earth's angular velocity of rotation. The labels path I and path II in equation (1) refer to the trajectories that the neutron follows through the interferometer neglecting the effects of gravity and the phase shifter. This perturbative method, based on the idea of Feynman–Dirac path integrals (Dirac, 1945; Feynman, 1948), is accurate to first order in the potential energy for potential energies small relative to the kinetic energy of the free particle as discussed by Greenberger & Overhauser (1979) and Opat (1995).

In the free space between the interferometer blades, the canonical momentum to first order in $\mathbf{g}$ is
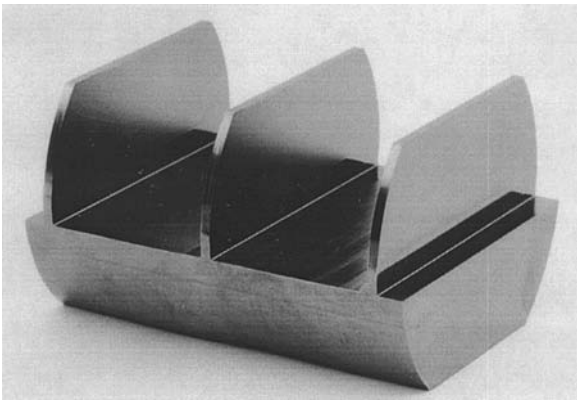

Fig. 3. A photograph of the symmetric interferometer used in this experiment. The blades of the interferometer are 3.077 mm thick and 50.404 mm apart. This interferometer was machined at Atominstitut, Vienna, Austria.

$$\mathbf{p} \cong m_i(v_0 - m_g\mathbf{g} \cdot \mathbf{x}/m_iv_0)\hat{\mathbf{l}} + m_i\omega \times \mathbf{x}, \qquad (3)$$

where m_g is the gravitational mass of the neutron, $\hat{\mathbf{l}}$ is the unit vector along its trajectory, $v_0 = 2\pi\hbar/m\lambda$ is its speed when it enters the interferometer and

$$\mathbf{g} = -[(GM/R^2)\hat{\mathbf{R}} + (m_i/m_g)\omega \times (\omega \times \mathbf{R})] \qquad (4)$$

is the classical effective acceleration due gravity felt by the neutron due to the combined action of the gravitational and centrifugal forces. Here, M is the mass of the Earth and $\mathbf{R}$ is the vector from the center of the Earth to the point at which the neutron enters the interferometer. Inside the aluminium phase-shifter slab, the canonical momentum is

$$\mathbf{p} \cong m_i[v_0 - (m_g\mathbf{g} \cdot \mathbf{x}/m_iv_0) - U_n/m_iv_0]\hat{\mathbf{l}} + m_i\omega \times \mathbf{x}. \qquad (5)$$

The neutron–nuclear optical potential U_n, related to the strong force of interaction between the neutron and the aluminium nuclei, is

$$U_n = 2\pi\hbar^2 Nb/m, \qquad (6)$$

where N is the number density of atoms in the aluminium and b is the average coherent neutron scattering length for the aluminium nuclei. Since, for $\lambda \simeq 2\,\text{Å}$ neutrons, $m_g g \simeq 1\,\text{meV cm}^{-1}$, $U_n \simeq 0.05\,\mu\text{eV}$ and $E = m_iv_0^2/2 \simeq 20\,\text{meV}$, the use of these approximate canonical momenta and the semiclassical perturbative approach for calculating the phase shifts as described by equation (1) is valid.

If we assume that the incident beam is level and all neutrons exactly satisfy the Bragg condition, gravity and the centrifugal force due to the Earth's rotation result in a phase shift of

$$\Delta\Phi_{\text{COW}} = (m_g/\hbar v)\left[\int_{\text{path II}} \mathbf{g} \cdot \mathbf{x}\,dl - \int_{\text{path I}} \mathbf{g} \cdot \mathbf{x}\,dl\right]$$
$$= -m_g g A_0 \sin\alpha/\hbar v_0$$
$$= -2\pi\lambda m_i m_g(g/h^2)A_0 \sin\alpha, \qquad (7)$$

where

$$A_0 = [2d_1d_2 + a(d_1 + d_2)]\tan\theta_B \qquad (8)$$

is the area enclosed by the trajectories of the neutrons (see Fig. 1) that exactly satisfy the Bragg condition along the two paths of the interferometer assuming no deflections due to potentials other than that of the interferometer itself, and θ_B is the Bragg angle for the mean neutron wavelength. We note that the area dependence of $\Delta\Phi_{\text{COW}}$ is a mathematical artifact of the Mach–Zehnder interferometer geometry. The fundamental quantity upon which this phase shift depends is the height of one path above the other. Thus, a gravitational phase shift will also be present in interferometers in other geometries such as the Michelson geometry where there is no area enclosed by the paths

of the interferometer but the average height of the neutrons along the two paths can vary. Equation (8) is presented for the more general situation of a skew-symmetric interferometer; for a symmetric interferometer $d_1 = d_2$. Equation (7) is frequently referred to as the COW formula (Colella *et al.*, 1975).

Since the experiment is performed in the Earth's rotating frame of reference, the Coriolis force on the moving neutron gives rise to a phase shift known as the Sagnac or Page effect (Sagnac, 1913*a,b*; Page, 1975; Anandan, 1979, 1981; Stodolsky, 1979). It is given by

$$\Delta\Phi_{\text{Sagnac}}(\alpha, \lambda) = (m_i/\hbar)\omega \cdot \left[\int\limits_{\text{path II}} \mathbf{x} \cdot d\mathbf{l} - \int\limits_{\text{path I}} \mathbf{x} \cdot d\mathbf{l} \right]$$
$$= (m_i/\hbar) \oint (\omega \times \mathbf{x}) \, d\mathbf{l}$$
$$= 2m_i\omega \cdot \mathbf{A}_0/\hbar, \qquad (9)$$

where $\mathbf{A}_0$ is the normal area vector corresponding to the loop in space whereby the neutron leaves the source along path II and returns to it *via* path I. Since, in the experiments at the MURR reactor in Missouri, the beam incident on the interferometer is oriented along a local North–South line and is level with respect to the Earth, the Sagnac phase shift for our experimental situation is

$$\Delta\Phi_{\text{Sagnac}} = -s \cos\alpha \tan\theta_B. \qquad (10)$$

The factor s is given by

$$s \equiv 2m_i\omega A_0 \cos\theta_L/\hbar \tan\theta_B, \qquad (11)$$

where $\theta_L = 51.37°$ is the colatitude angle for Columbia, Missouri. Since previous experiments (Werner *et al.*, 1979; Atwood *et al.*, 1984) have shown that the Sagnac phase shift agrees with theory to within the accuracy of the experimental data, we treat it as a known quantity. Its magnitude is about 2% of the phase shift due to gravity.

The phase shift due to the aluminium phase shifter is determined by the difference in the thicknesses of aluminium along the two paths. From the geometry of the experiment, this nuclear phase shift is

$$\Delta\Phi_{\text{nuc}}(\delta, \lambda) = \lambda NbD[1/\cos(\theta_B + \delta) - 1/\cos(\theta_B - \delta)], \qquad (12)$$

where D is the thickness of the phase shifter and δ is the angle through which it is rotated defined as shown in Fig. 1.

The interferometers are inevitably somewhat strained as a result of the process of machining with diamond cutting wheels, even after etching, and the way in which they are mounted in the apparatus. They can also deform under their own weight when tilted. We have assumed for the purpose of our analysis of the experimental results that the only effects of bending and strains on the phase are the result of a slightly longer free-space path length in one path of the interferometer than in the other. This produces a phase shift of

$$\Delta\Phi_{\text{bend}}(\alpha, \lambda) = 2\pi\lambda^{-1}\Delta l(\alpha), \qquad (13)$$

where $\Delta l(\alpha)$ is the amount that path II is longer than path I due to bending.

3. Single-crystal amplitudes

In order to describe the effects of dynamical diffraction in the interferometer, we need to discuss the reflection and transmission coefficients due to diffraction in each crystal. Consider a plane-wave component of the incident beam with a wavevector $\mathbf{k}$ in free space such that it is incident on the first blade of the interferometer at an angle slightly less than the Bragg angle. In this situation, the off-Bragg parameter y, defined by

$$y = (-2\mathbf{k} \cdot \mathbf{g} + \mathbf{G} \cdot \mathbf{G})/(4m|V_{\mathbf{G}}|/\hbar^2) = -\Delta\theta\Lambda_0/d_{hkl}, \qquad (14)$$

is positive. This parameter is used to characterize the deviation $\Delta\theta$ from the exact Bragg condition and determines the paths along which this plane-wave component travels through the interferometer as it is diffracted by the crystal lattice planes of reciprocal-lattice vector $\mathbf{G}$. In this expression, $V_{\mathbf{G}}$ is the Fourier component of the neutron interaction potential with the silicon crystal corresponding to $\mathbf{G}$, $\Lambda_0 = \pi\hbar^2 k \cos\theta_B/m_i|V_{\mathbf{G}}|$ is the *Pendellösung* length and d_{hkl} is the spacing between the diffracting lattice planes. Here, $k = 2\pi/\lambda$ is the modulus of $\mathbf{k}$, the incident neutron wavevector. Dynamical diffraction within the crystal produces two neutron current branches associated with this component, labeled α and β, as shown in Fig. 4. These current branches traverse the crystal at angles $\pm\Omega$ relative to the diffracting planes. The value of Ω is determined in terms of y by the relation

$$\tan\Omega = \Gamma \tan\theta_B, \qquad (15)$$

where

$$\Gamma \equiv y(1 + y^2)^{-1/2}. \qquad (16)$$

Since the amount that the currents for a given value of the y parameter are displaced along the exit face of a crystal of thickness a relative to the currents when $y = 0$, given by

$$\Delta x = a\Gamma \tan\theta_B, \qquad (17)$$

is proportional to the dimensionless parameter Γ, we will use Γ to provide a scale to describe beam profiles on the exit crystal surfaces. At the exit face of the crystal, each current branch releases two waves, one with its wavevector in the $\mathbf{O}$ or incident direction and the other in the $\mathbf{G}$ or diffracted direction.

The situation in the first blade of the interferometer is illustrated in Fig. 4(*a*). The situation in the intermediate

or mirror blade in path I and the final or analyzer blade in path II is the same. For the second reflection along each path, at the mirror blade in path II and the analyzer blade in path I, the situation differs as illustrated in Fig. 4(b). For this situation, the reciprocal-lattice vector is now $-\mathbf{G}$ and $\Delta\theta$ is positive so that y and thus Γ are both negative. The reflection and transmission coefficients describing the amplitudes of these waves as determined from the dynamical theory of diffraction are given in Table 1.

In his original analysis, Horne (1986) assumed that the incident beam illuminates the interferometer through a slit that is much larger than the average neutron wavelength, so that single-slit diffraction can be ignored, but much smaller than the thickness of the crystal, so that the α and β branches arising from a single point on the front surface of a crystal blade are physically separated and thus do not interfere with each other at the back surface. Although the first assumption is certainly valid for the experimental conditions of neutron gravitational phase shift measurements, the second often is not. However, this argument may still be valid as the blade
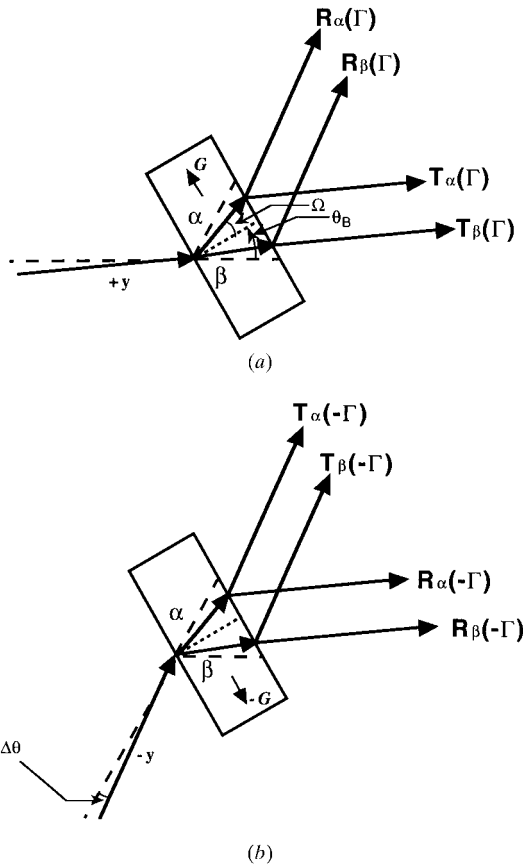
Table 1. *Functional dependence of the a and b current branch reflection and transmission coefficients on Γ*

Coefficient	Amplitude
$R_\alpha(\Gamma)$	$\frac{1}{2}(1-\Gamma^2)^{1/2}$
$R_\beta(\Gamma)$	$-\frac{1}{2}(1-\Gamma^2)^{1/2}$
$T_\alpha(\Gamma)$	$\frac{1}{2}(1-\Gamma)$
$T_\beta(\Gamma)$	$\frac{1}{2}(1+\Gamma)$

thickness is much greater than the transverse coherence length (Rauch *et al.*, 1996) of the incident neutrons. Since the relative strengths of the independent α and β neutron current branches are determined at the surface at which the neutron enters the crystal, the internal *Pendellösung* interference current present in the crystal can be disregarded in the calculation of the trajectories of the neutrons within the crystal as it represents the results of the superposition of the two current branches, not an exchange of neutrons between them.

4. Theoretical gravity interferogram

The beam geometry as predicted by the dynamical diffraction theory for a skew-symmetric interferometer is shown in Fig. 5. Instead of only two paths through the interferometer, there are in reality 16 different paths for each value of Γ leading to the four points labeled a, b, c and d at positions on the exit face of the analyzer blade $\Gamma_A = 3\Gamma, \Gamma, -\Gamma$ and -3Γ, respectively. Each of the eight numbered paths in the two intermediate mirror crystals contributes intensity to two of the exit points. The pairs of paths leading to the exit points a and d, referred to as *maverick paths* (Horne, 1986), travel along either the α or the β current branch exclusively in all three crystals. The sets of six paths leading to points b and c travel along both α and β branches with the same number of each for all paths along both beams leading to the same exit point. These paths are referred to as the *primary paths*.

Fig. 4. Diagram showing the four waves present in a blade of the interferometer for neutrons with incident off-Bragg parameter y positive (a) before reflection (initial incidence or after two reflections) and (b) after one reflection.
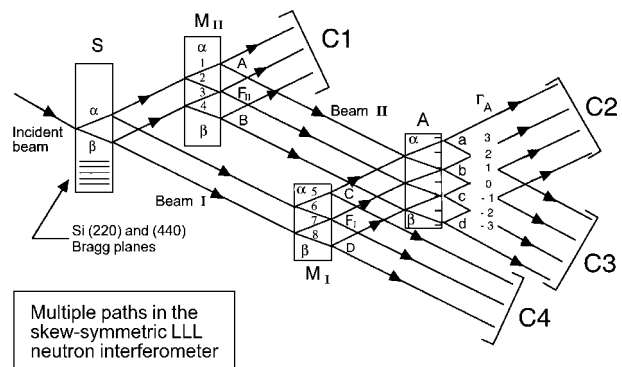

Fig. 5. A diagram of the 16 possible paths through the interferometer predicted by dynamical diffraction theory. Paths exiting the interferometer at the same point on the analyzer blade interfere with each other but do not interfere coherently with paths exiting at other points.

Table 2. *Amplitudes and accumulated phases of the paths in the C2 detector beam that exit the analyzer blade of the interferometer at points a and b as shown in Fig. 5*

Path	Coefficient	Amplitude	Phase
1a	$R_\alpha(\Gamma)R_\alpha(-\Gamma)R_\alpha(\Gamma)$	$\frac{1}{8}(1-\Gamma^2)^{3/2}$	$\Delta\Phi_0/2 + \Gamma\sigma$
5a	$T_\alpha(\Gamma)R_\alpha(\Gamma)T_\alpha(-\Gamma)$	$\frac{1}{8}(1-\Gamma^2)^{3/2}$	$-\Delta\Phi_0/2 - \Gamma\sigma$
1b	$R_\alpha(\Gamma)R_\alpha(-\Gamma)R_\beta(\Gamma)$	$-\frac{1}{8}(1-\Gamma^2)^{3/2}$	$\Delta\Phi_0/2 + \Gamma(\chi+\sigma)$
2b	$R_\alpha(\Gamma)R_\beta(-\Gamma)R_\alpha(\Gamma)$	$-\frac{1}{8}(1-\Gamma^2)^{3/2}$	$\Delta\Phi_0/2 - \Gamma\sigma$
3b	$R_\beta(\Gamma)R_\alpha(-\Gamma)R_\alpha(\Gamma)$	$-\frac{1}{8}(1-\Gamma^2)^{3/2}$	$\Delta\Phi_0/2 - \Gamma(\chi-\sigma)$
5b	$T_\alpha(\Gamma)R_\alpha(\Gamma)T_\beta(-\Gamma)$	$\frac{1}{8}(1-\Gamma^2)^{1/2}(1-\Gamma)^2$	$-\Delta\Phi_0/2 + \Gamma(\chi-\sigma)$
6b	$T_\alpha(\Gamma)R_\beta(\Gamma)T_\alpha(-\Gamma)$	$-\frac{1}{8}(1-\Gamma^2)^{3/2}$	$-\Delta\Phi_0/2 + \Gamma\sigma$
7b	$T_\beta(\Gamma)R_\alpha(\Gamma)T_\alpha(-\Gamma)$	$\frac{1}{8}(1-\Gamma^2)^{1/2}(1+\Gamma)^2$	$-\Delta\Phi_0/2 - \Gamma(\chi+\sigma)$
4d	$R_\beta(\Gamma)R_\beta(-\Gamma)R_\beta(\Gamma)$	$-\frac{1}{8}(1-\Gamma^2)^{3/2}$	$\Delta\Phi_0/2 - \Gamma\sigma$
8d	$T_\beta(\Gamma)R_\beta(\Gamma)T_\beta(-\Gamma)$	$-\frac{1}{8}(1-\Gamma^2)^{3/2}$	$-\Delta\Phi_0/2 + \Gamma\sigma$
4c	$R_\beta(\Gamma)R_\beta(-\Gamma)R_\alpha(\Gamma)$	$\frac{1}{8}(1-\Gamma^2)^{3/2}$	$\Delta\Phi_0/2 - \Gamma(\chi+\sigma)$
3c	$R_\beta(\Gamma)R_\alpha(-\Gamma)R_\beta(\Gamma)$	$\frac{1}{8}(1-\Gamma^2)^{3/2}$	$\Delta\Phi_0/2 + \Gamma\sigma$
2c	$R_\alpha(\Gamma)R_\beta(-\Gamma)R_\beta(\Gamma)$	$\frac{1}{8}(1-\Gamma^2)^{3/2}$	$\Delta\Phi_0/2 + \Gamma(\chi-\sigma)$
8c	$T_\beta(\Gamma)R_\beta(\Gamma)T_\alpha(-\Gamma)$	$-\frac{1}{8}(1-\Gamma^2)^{1/2}(1+\Gamma)^2$	$-\Delta\Phi_0/2 - \Gamma(\chi-\sigma)$
7c	$T_\beta(\Gamma)R_\alpha(\Gamma)T_\beta(-\Gamma)$	$\frac{1}{8}(1-\Gamma^2)^{3/2}$	$-\Delta\Phi_0/2 - \Gamma\sigma$
6c	$T_\alpha(\Gamma)R_\beta(\Gamma)T_\beta(-\Gamma)$	$-\frac{1}{8}(1-\Gamma^2)^{1/2}(1-\Gamma)^2$	$-\Delta\Phi_0/2 + \Gamma(\chi+\sigma)$

The phase accumulated by the neutron along each of these paths is calculated by the use of equation (1). The amplitudes and phase shifts for the 16 paths leading to points *a*, *b*, *c* and *d* are presented in Table 2 for the C2 (or **G**) beam and in Table 3 for the C3 (or **O**) beam. In these tables, the label 1*a* means path 1 through the middle mirror crystal and point *a* on the analyzer crystal; path 1*b* means path 1 through the middle mirror crystal and point *b* on the analyzer crystal, and so on. The phase shift

$$\Delta\Phi_0(\alpha, \delta) = \Delta\Phi_{\text{COW}}(\alpha) + \Delta\Phi_{\text{nuc}}(\delta) \qquad (18)$$

refers to the gravity-induced and nuclear phase shifts when the Bragg condition is exactly satisfied as described above by equations (7) and (12), respectively. The term χ is the average gravitational phase shift due to the area between the adjacent paths comprising either of the subbeams (labeled beam I and beam II in Fig. 5) at $\Gamma = 1$ and is given by the expression

$$\chi(\alpha)[a(d_1 + d_2) + 2a^2]\tan\theta_B\Delta\Phi_{\text{COW}}(\alpha)/A_0. \qquad (19)$$

The term

$$\sigma(\alpha) = a(d_2 - d_1)\tan\theta_B\Delta\Phi_{\text{COW}}(\alpha)/2A_0 \qquad (20)$$

represents corrections to the gravity-induced phase shift due to asymmetry of the interferometer. We have taken into account the reduced effective speed of the neutron while diffracting in the crystal (Shull *et al.*, 1980),

$$v' = v_0 \cos\theta_B/\cos\Omega, \qquad (21)$$

in calculating these phase shifts. A very simplified explanation for both the effective velocity and the need to account for it in these calculations is that the neutron can be thought of as traveling with constant speed within the the crystal and being either reflected or transmitted by each set of crystal planes that it encounters, with the strengths of the reflection and transmission coefficients dependent on Γ. In this picture, the neutron trajectories described here are the weighted average of all possible trajectories of neutrons with that value of Γ and thus neglect the rapid changes in trajectory due to reflection, reducing to a straight line. However, since all neutrons actually have the same optical path length within the crystal, the time required to transit the crystal is the same, giving rise to the effective velocity described by equation (21). For the special case of a symmetric interferometer ($d_1 = d_2$), $\sigma = 0$ and χ simplifies to

$$\chi(\alpha) = (a/d_1)\Delta\Phi_{\text{COW}}(\alpha). \qquad (22)$$

The phase shifts due to the Sagnac effect and bending have been omitted. The phase shifts *common to all paths in both beams* leading to the same exit point such as the *Pendellösung* phases due to α and β branch diffraction and the gravitational phase shift due to the height difference between the entrance and exit points are also not included in the table.

The amplitudes and phase shifts for the paths terminating at points *c* and *d* display the symmetry of the problem in the following manner: If the incident Γ is negative, the sets of paths leading to points *c* and *d* overlay the paths leading to points *b* and *a* for the corresponding positive incident Γ, respectively. Thus, the phase accumulated along these paths is identical to the phase accumulated in the corresponding paths for positive incident Γ. The amplitudes along these paths are determined by replacing the α and β branch reflection and transmission coefficients for the corresponding path with positive incident Γ with the band α branch coefficients, respectively, and reversing the sign of Γ for each coefficient. The amplitudes of the paths for incident negative Γ are identical to their counterparts for a positive Γ in the paths leading to the C3 detector and equal in magnitude and opposite in sign for those leading to the C2 detector since each modification of a reflection coefficient produces a change of sign. Likewise, the phase accumulated along the trajectories

Table 3. *Amplitudes and accumulated phases of the paths in the C3 detector beam that exit the analyzer blade of the interferometer at points a and b as shown in Fig. 5*

Path	Coefficient	Amplitude	Phase
1a	$R_\alpha(\Gamma)R_\alpha(-\Gamma)T_\alpha(\Gamma)$	$\frac{1}{8}(1-\Gamma^2)(1-\Gamma)$	$\Delta\Phi_0/2 + \Gamma\sigma$
5a	$T_\alpha(\Gamma)R_\alpha(\Gamma)R_\alpha(-\Gamma)$	$\frac{1}{8}(1-\Gamma^2)(1-\Gamma)$	$-\Delta\Phi_0/2 - \Gamma\sigma$
1b	$R_\alpha(\Gamma)R_\alpha(-\Gamma)T_\beta(\Gamma)$	$\frac{1}{8}(1-\Gamma^2)(1+\Gamma)$	$\Delta\Phi_0/2 + \Gamma(\chi+\sigma)$
2b	$R_\alpha(\Gamma)R_\beta(-\Gamma)T_\alpha(\Gamma)$	$-\frac{1}{8}(1-\Gamma^2)(1-\Gamma)$	$\Delta\Phi_0/2 - \Gamma\sigma$
3b	$R_\beta(\Gamma)R_\alpha(-\Gamma)T_\alpha(\Gamma)$	$-\frac{1}{8}(1-\Gamma^2)(1-\Gamma)$	$\Delta\Phi_0/2 - \Gamma(\chi-\sigma)$
5b	$T_\alpha(\Gamma)R_\alpha(\Gamma)R_\beta(-\Gamma)$	$-\frac{1}{8}(1-\Gamma^2)(1-\Gamma)$	$-\Delta\Phi_0/2 + \Gamma(\chi-\sigma)$
6b	$T_\alpha(\Gamma)R_\beta(\Gamma)R_\alpha(-\Gamma)$	$-\frac{1}{8}(1-\Gamma^2)(1-\Gamma)$	$-\Delta\Phi_0/2 + \Gamma\sigma$
7b	$T_\beta(\Gamma)R_\alpha(\Gamma)R_\alpha(-\Gamma)$	$\frac{1}{8}(1-\Gamma^2)(1+\Gamma)$	$-\Delta\Phi_0/2 - \Gamma(\chi+\sigma)$
4d	$R_\beta(\Gamma)R_\beta(-\Gamma)T_\beta(\Gamma)$	$\frac{1}{8}(1-\Gamma^2)(1+\Gamma)$	$\Delta\Phi_0/2 - \Gamma\sigma$
8d	$T_\beta(\Gamma)R_\beta(\Gamma)R_\beta(-\Gamma)$	$\frac{1}{8}(1-\Gamma^2)(1+\Gamma)$	$-\Delta\Phi_0/2 + \Gamma\sigma$
4c	$R_\beta(\Gamma)R_\beta(-\Gamma)T_\alpha(\Gamma)$	$\frac{1}{8}(1-\Gamma^2)(1-\Gamma)$	$\Delta\Phi_0/2 - \Gamma(\chi+\sigma)$
3c	$R_\beta(\Gamma)R_\alpha(-\Gamma)T_\beta(\Gamma)$	$-\frac{1}{8}(1-\Gamma^2)(1+\Gamma)$	$\Delta\Phi_0/2 + \Gamma\sigma$
2c	$R_\alpha(\Gamma)R_\beta(-\Gamma)T_\beta(\Gamma)$	$-\frac{1}{8}(1-\Gamma^2)(1+\Gamma)$	$\Delta\Phi_0/2 + \Gamma(\chi-\sigma)$
8c	$T_\beta(\Gamma)R_\beta(\Gamma)R_\alpha(-\Gamma)$	$-\frac{1}{8}(1-\Gamma^2)(1+\Gamma)$	$-\Delta\Phi_0/2 - \Gamma(\chi-\sigma)$
7c	$T_\beta(\Gamma)R_\alpha(\Gamma)R_\beta(-\Gamma)$	$-\frac{1}{8}(1-\Gamma^2(1+\Gamma)$	$-\Delta\Phi_0/2 - \Gamma\sigma$
6c	$T_\alpha(\Gamma)R_\beta(\Gamma)R_\beta(-\Gamma)$	$\frac{1}{8}(1-\Gamma^2)(1-\Gamma)$	$-\Delta\Phi_0/2 + \Gamma(\chi+\sigma)$

leading to points *c* and *d* for positive Γ are the same as those accumulated along those leading to points *b* and *a* for negative Γ. The amplitudes are of equal magnitude and opposite sign for the C2 detector beam and identically equal for the C3 beam.

In order to calculate the intensity profiles and integrated intensities of the exit beams for the interferometer, we assume that the angular divergence of the incident beam is broad in comparison to the Darwin width or, alternatively, the distribution of the neutrons in the incident beam as a function of their incident off-Bragg parameter *y* is given by

$$P(y) = 1. \tag{23}$$

Note that the definition of $P(y)$ is not a probability as it is not normalized but instead is a statement that all possible values of *y* are equally likely. Although this assumption leads to the unphysical results that the integrated intensities of both the incident beam and the C4 beam are infinite, it is not unreasonable in that the distribution in wavevector of neutrons incident on the interferometer is much broader than the range of wavevectors for neutrons that participate in interference and is approximately constant across this range. Neutrons traveling along the paths leading to each of the exit points interfere with each other but not with neutrons that travel to different points as the neutron wave packets, as determined by the transverse coherence length, do not overlap. Although neutrons incident with an off-Bragg parameter of $-y$ have the same trajectories to the same exit points as those with an off-Bragg parameter of $+y$, they will not interfere with each other as they are assumed to arise from separate and distinct plane-wave components coming from the monochromator with no fixed phase relationship. Since Γ is related to *y* as given in equation (16), the distribution of the incident neutrons as a function of Γ is

$$P(\Gamma) = P(y)|dy/d\Gamma| = (1-\Gamma^2)^{-3/2}. \tag{24}$$

In calculating the total intensity measured by the detectors, we assume that all neutrons from all four exit points are accepted and detected by either the C2 or C3 detector. With these assumptions, the contribution to the total intensity measured in the C2 detector due to the component of the incident beam with a given value of Γ and an interferometer tilt angle α is given by

$$
\begin{aligned}
I_{C2}(\alpha, \Gamma) = &\tfrac{1}{32}(1-\Gamma^2)^{-1/2}\{(1+\Gamma)^4 + (1-\Gamma)^4 \\
&+ 2(1-\Gamma^2)^2(3 + 2\cos 2\Gamma\chi) \\
&- 4\Gamma^2(1-\Gamma^2)[\cos\Gamma(\chi-2\sigma) \\
&+ \cos\Gamma(\chi+2\sigma)]\} \\
&- \tfrac{1}{16}(1-\Gamma^2)^{1/2}\cos\Delta\Phi_0\{4\Gamma^2(\cos\Gamma\chi \\
&+ \cos\Gamma\sigma) + (1+\Gamma^2)[\cos 2\Gamma(\chi+\sigma) \\
&+ \cos 2\Gamma(\chi-\sigma)]\} \\
&+ (\Gamma/8)(1-\Gamma^2)^{1/2}\sin\Delta\Phi_0\{2\sin\Gamma\chi \\
&+ [\sin 2\Gamma(\chi+\sigma) + 2\Gamma(\chi-\sigma)]\}.
\end{aligned}
\tag{25}
$$

Likewise, the distribution of the intensity measured in the C3 detector as a function of incident Γ is given by

$$
\begin{aligned}
I_{C3}(\alpha, \Gamma) = &\tfrac{1}{8}(1-\Gamma^2)(1+\Gamma^2)^{1/2}\{2(1+\Gamma^2) \\
&- (1-\Gamma^2)\cos 2\Gamma\chi + (1+\Gamma^2)\cos\Gamma(\chi-2\sigma) \\
&- (1-\Gamma^2)\cos\Gamma(\chi+2\sigma)\} \\
&+ \tfrac{1}{16}(1-\Gamma^2)^{1/2}\cos\Delta\Phi_0\{4\Gamma^2(\cos\Gamma\chi \\
&+ \cos\Gamma\sigma) + (1+\Gamma^2)[\cos 2\Gamma(\chi+\sigma) \\
&+ \cos 2\Gamma(\chi-\sigma)]\} - (\Gamma/8)(1-\Gamma^2)^{1/2} \\
&\times \sin\Delta\Phi_0\{2\sin\Gamma\chi + [\sin 2\Gamma(\chi+\sigma) \\
&+ \sin 2\Gamma(\chi-\sigma)]\}.
\end{aligned}
\tag{26}
$$

The intensity distributions given by equations (25) and (26) are even functions of Γ due to the relationships

between the amplitudes and phases at the four exit points. Although the explicit dependence of the intensity in the C2 detector on the phase factor $\Delta\Phi_0$ is equal and opposite to that of the intensity in the C3 detector, the two intensities do not sum to a constant value as the mean intensities measured in the two detectors depend differently on the tilt angle α.

It is also interesting to consider the distribution of intensity accepted by the detectors as a function of the position of the exit point Γ_A on the analyzer blade. The distribution of neutrons as a function of Γ_A along any given path based on the assumed incident spectrum ignoring the dependence on y or Γ of the amplitude of that path is

$$P_p(\Gamma_A) = (1 - \Gamma_A^2)^{-3/2} \qquad (27)$$

for the primary paths, and

$$P_M(\Gamma_A) = \tfrac{1}{3}[1 - (\Gamma_A/3)^2]^{-3/2} \qquad (28)$$

for the maverick paths, based on the values of Γ_A in terms of the incident Γ at the exit points. Thus, the distribution of intensity across the beam to the C2 detector is given by

$$
\begin{aligned}
I_{C2P}(\alpha, \Gamma_A) = & \tfrac{1}{32}(1 - \Gamma_A^2)^{-1/2}\{(1 + \Gamma_A)^4 + 4(1 - \Gamma_A^2)^2 \\
& \times (1 + \cos 2\Gamma_A \chi) + (1 - \Gamma_A)^4 \\
& + 4\Gamma_A(1 - \Gamma_A^2)[(1 - \Gamma_A)\cos\Gamma_A(\chi - 2\sigma) \\
& - (1 + \Gamma_A)\cos\Gamma_A(\chi + 2\sigma)]\} \\
& - \tfrac{1}{16}(1 - \Gamma_A^2)^{1/2}\cos\Delta\Phi_0\{(1 + 3\Gamma_A^2) \\
& \times \cos\Gamma_A\sigma + 4\Gamma_A^2\cos\Gamma_A\chi \\
& + (1 + \Gamma_A)^2\cos 2\Gamma_A(\chi + \sigma) \\
& + (1 - \Gamma_A)^2\cos 2\Gamma_A(\chi - \sigma)\} \\
& + \tfrac{1}{16}(1 - \Gamma_A^2)^{1/2}\sin\Delta\Phi_0\{(3\Gamma_A^2 + 1) \\
& \times \sin 2\Gamma_A\sigma + 4\Gamma_A\sin\Gamma\chi \\
& + (1 + \Gamma_A)^2\sin 2\Gamma_A(\chi + \sigma) \\
& + (1 - \Gamma_A)^2\sin 2\Gamma_A(\chi - \sigma)\} \qquad (29)
\end{aligned}
$$

due to the primary paths, and

$$
\begin{aligned}
I_{C2M}(\alpha, \Gamma_A) = & \tfrac{1}{48}[1 - (\Gamma_A/3)^2]^{3/2} \\
& \times [1 - \cos\Delta\Phi_0\cos(2\Gamma_A\sigma/3) \\
& + \sin\Delta\Phi_0\sin(2\Gamma_A\sigma/3)] \qquad (30)
\end{aligned}
$$

due to the maverick paths. Likewise, the contributions to the intensity profile of the C3 beam due to the primary and maverick paths are given by

$$
\begin{aligned}
I_{C3P}(\alpha, \Gamma_A) = & \tfrac{1}{16}(1 - \Gamma_A^2)^{1/2}\{2(1 - \Gamma_A)^2 - 4(1 - \Gamma_A^2) \\
& \times \cos 2\Gamma_A\chi + (1 + \Gamma_A)^2 \\
& + 4(1 - \Gamma_A)^2\cos\Gamma_A(\chi - 2\sigma) \\
& - 4(1 - \Gamma_A^2)\cos\Gamma_A(\chi + 2\sigma)\} \\
& + \tfrac{1}{16}(1 - \Gamma_A^2)^{1/2}\cos\Delta\Phi_0\{(3\Gamma_A^2 - 2\Gamma_A - 1) \\
& \times \cos\Gamma_A\sigma + (4\Gamma_A^2 - 2\Gamma_A)\cos\Gamma_A\chi \\
& + (1 + \Gamma_A)^2\cos 2\Gamma_A(\chi + \sigma) \\
& + (1 - \Gamma_A)^2\cos 2\Gamma_A(\chi - \sigma)\} \\
& + \tfrac{1}{16}(1 - \Gamma_A^2)^{1/2}\sin\Delta\Phi_0\{(3 - 2\Gamma_A^2 - \Gamma_A^2) \\
& \times \sin 2\Gamma_A\sigma + 4(1 - \Gamma_A)\sin\Gamma\chi \\
& + (1 + \Gamma_A)^2\sin 2\Gamma_A(\chi + \sigma) \\
& + (1 - \Gamma_A)^2\sin 2\Gamma_A(\chi - \sigma)\} \qquad (31)
\end{aligned}
$$

and

$$
\begin{aligned}
I_{C3M}(\alpha, \Gamma_A) = & \tfrac{1}{48}[1 - (\Gamma_A/3)^2]^{1/2}(1 - \Gamma_A/3)^2 \\
& \times [1 - \cos\Delta\Phi_0\cos(2\Gamma_A\sigma/3) \\
& + \sin\Delta\Phi_0\sin(2\Gamma_A\sigma/3)], \qquad (32)
\end{aligned}
$$

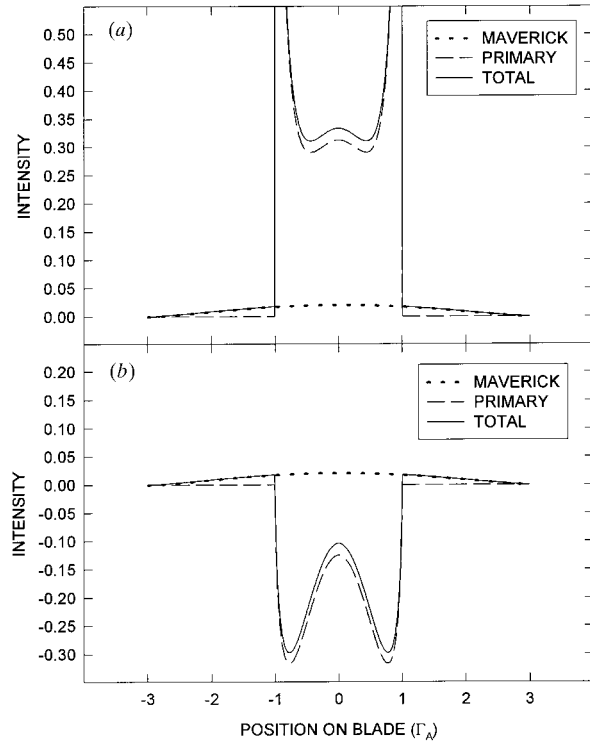respectively. The intensity profiles in the beam leading to the C2 detector can be written in the form

Fig. 6. Contributions of the maverick- and primary-path intensity profiles to the total C2 detector intensity profile at tilt $\alpha = 0°$: (a) mean intensity profile; (b) oscillation amplitude profile.

$$I_{C2}(\alpha, \Gamma_A) = A_{C2}(\alpha, \Gamma_A) - B_{C2}(\alpha, \Gamma_A)$$
$$\times \cos[\Delta\Phi_0 + \Delta\Phi_{C2}(\alpha, \Gamma_A)], \quad (33)$$

where A_{C2} is the mean intensity, B_{C2} is the amplitude of oscillation due to changes in $\Delta\Phi_0$ and $\Delta\Phi_{C2}$ is the additional phase correction due to dynamical diffraction. Likewise, the intensity profile in the C3 beam is given by

$$I_{C3}(\alpha, \Gamma_A) = A_{C3}(\alpha, \Gamma_A) - B_{C3}(\alpha, \Gamma_A)$$
$$\times \cos[\Delta\Phi_0 + \Delta\Phi_{C3}(\alpha, \Gamma_A)]. \quad (34)$$

The mean intensity and oscillation amplitude profiles and the contributions to each from the primary and maverick paths when the interferometer is level are shown in Fig. 6 for the C2 beam and Fig. 7 for the C3 beam. These profiles, which are independent of the interferometer used, are identical to those calculated from the spherical-wave dynamical diffraction theory (Petrascheck & Folk, 1976; Petrascheck, 1979). While the amplitude of oscillation and the mean intensity distribution across the beam are the same (at $\alpha = 0°$) for C3, they are different for the C2 beam. Also, the contributions to the amplitude of oscillation of the primary and maverick paths for the C3 detector and the primary path for C2 are positive but the contribution of the maverick paths to the C2 amplitude of oscillation is negative. Thus, the oscillations in the C2 intensity due to $\Delta\Phi_0$ from the maverick paths are in phase with those in the C3 intensity while those from the primary paths are π rad out of phase. Although the intensities in the two detectors are even functions of the incident spectrum as determ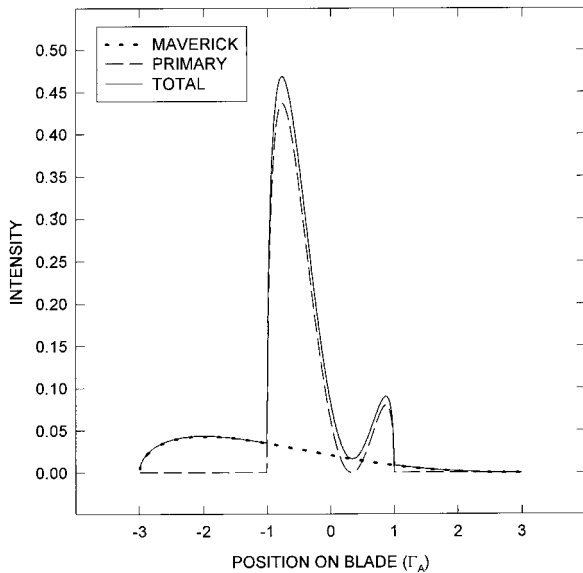ined by Γ, the profiles of the intensities as a function of Γ_A are asymmetric and have different amplitudes of oscillation.

The difference in sign between the amplitudes of oscillation in intensity due to the primary and maverick paths explains one of the fundamental differences between X-ray and neutron interference and may explain an interesting feature noted in some neutron phase rotator scans. In neutron phase rotator scans, the intensity measured by the C2 detector is observed to oscillate π rad out of phase with that measured by the C3 detector while in X-ray phase rotator scans the two intensities oscillate in phase. The path analysis presented here is just as valid for X-rays as it is for neutrons but it fails to take into account the effects of absorption. Since silicon is a strong X-ray absorber, only the X-rays on one current branch, the branch with wavefunction nodes located at the Si atoms, can pass through the interferometer without being absorbed. Thus all X-rays counted in the C2 or C3 detectors followed the maverick trajectories. As noted before, the intensities of the C2 and C3 maverick paths oscillate in phase. Similarly, we would expect the intensity in the C2 detector in a neutron experiment to oscillate in phase with that measured in the C3 detector if the C2 detector were masked to exclude neutrons exiting the analyzer crystal in the range $-1 \leq \Gamma_A \leq 1$.

This difference may also explain an interesting feature noted in some neutron phase rotator scans. In many phase rotator scans such as the one shown in Fig. 8, the observed amplitude of oscillation in the C2
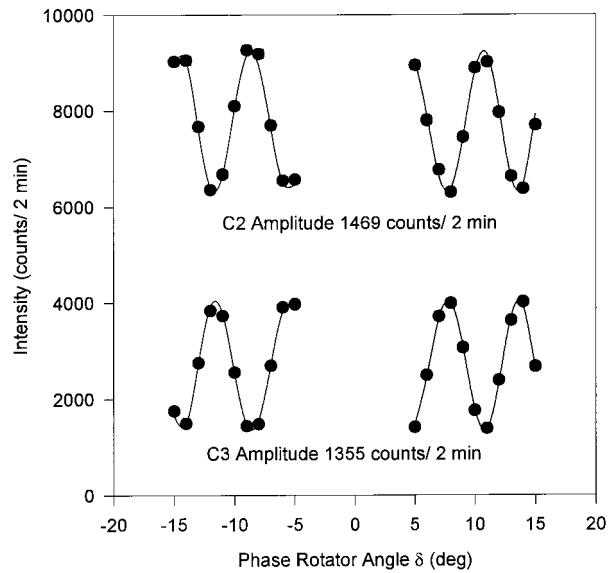

Fig. 7. Contributions of the maverick- and primary-path intensity profiles to the total C3 detector intensity profile at tilt $\alpha = 0°$. The mean intensity and oscillation amplitude profiles are the same.

Fig. 8. A sample interferogram measured by rotating the aluminium phase shifter with α fixed. The interferogram is split to maximize the phase accuracy of the fit while minimizing counting time. Note the higher amplitude of oscillation in the C2 detector. A possible explanation of this is given in the text.

detector is slightly larger than that observed in the C3 detector even though the C3 detector interferogram can in principle have perfect visibility while the C2 detector interferogram cannot. The amplitude of intensity oscillations is equal and opposite in the two detectors if all neutrons are accepted by both detectors. However, if the C2 detector is slightly misaligned so that some maverick-path neutrons are excluded, the intensity amplitude oscillations will be enhanced as the maverick intensity interferes destructively with the larger primary intensity. Similarly, if the C3 detector is slightly misaligned, the intensity amplitude oscillations will be damped since the maverick intensity interferes constructively with the primary intensity.

The profiles of the mean intensity, amplitude of oscillation and the phase-shift correction due to dynamical diffraction are all dependent on the interferometer tilt angle α or, equivalently, the COW formula gravitational phase shift $\Delta\Phi_{COW}$. Profiles of the mean intensities in the C2 and C3 detectors for various values of $\Delta\Phi_{COW}$ are shown in Figs. 9 and 10, respectively. Interference between the primary paths produces a richer structure of the profile and shifts the weight of the intensity distribution towards the center of the profile as $\Delta\Phi_{COW}$ increases. Profiles of the magnitudes of the amplitudes of oscillation $|B_{C2}|$ and $|B_{C3}|$ are shown in Figs. 11 and 12.

Since we have assumed that all neutrons in the C2 and C3 beams are accepted and counted by the detectors, the total intensity as measured by the detectors can be thought of as either the sum of the intensities contributed by all values of Γ in the incident beam or as the sum

of the intensity across the beam profile. These sums can be calculated analytically by the use of the following integrals:

$$F_1(\xi) \equiv \int_{-1}^{1} \Gamma^2 (1 - \Gamma^2)^{1/2} \cos(\xi\Gamma)\, d\Gamma$$
$$= \pi\xi^{-3}[3\xi J_0(\xi) - (6 - \xi^2) J_1(\xi)], \qquad (35)$$

$$F_2(\xi) \equiv \int_{-1}^{1} \Gamma (1 - \Gamma^2)^{1/2} \sin(\xi\Gamma)\, d\Gamma$$
$$= \pi\xi^{-2}[2J_1(\xi) - \xi J_0(\xi)], \qquad (36)$$

$$F_3(\xi) \equiv \int_{-1}^{1} (1 - \Gamma^2)^{1/2} \cos(\xi\Gamma)\, d\Gamma$$
$$= \pi\xi^{-1} J_1(\xi). \qquad (37)$$

Here $J_n(\xi)$ are the ordinary Bessel functions of order n and argument ξ. Thus, the total intensity in the C2 and C3 detectors as functions of the tilt angle α are given by

$$\begin{aligned}
\mathscr{I}_{C2}(\alpha) &= \int_{-1}^{1} I_{C2}(\alpha, \Gamma)\, d\Gamma \\
&= \int_{-1}^{1} I_{C2P}(\alpha, \Gamma_A)\, d\Gamma_A + \int_{-3}^{3} I_{C2M}(\alpha, \Gamma_A)\, d\Gamma_A \\
&= (11\pi/32) - \tfrac{1}{8}[F_1(\chi + 2\sigma) + F_1(\chi - 2\sigma) \\
&\quad + F_1(2\chi) - F_3(2\chi)] - \tfrac{1}{16}\cos\Delta\Phi_0 \\
&\quad \times \{4F_1(2\sigma) + 4F_1(\chi) + F_1[2(\chi + \sigma)] \\
&\quad + F_1[2(\chi - \sigma)] + F_3[2(\chi + \sigma)] + F_3[2(\chi - \sigma)]\} \\
&\quad + \tfrac{1}{8}\sin\Delta\Phi_0\{2F_2(\chi) + F_2[2(\chi + \sigma)] \\
&\quad + F_2[2(\chi - \sigma)]\} \qquad (38)
\end{aligned}$$

and

$$\begin{aligned}
\mathscr{I}_{C3}(\alpha) &= (5\pi/32) + \tfrac{1}{8}[F_1(\chi + 2\sigma) + F_1(\chi - 2\sigma) \\
&\quad + F_1(2\chi) + F_3(\chi - 2\sigma) - F_3(\chi + 2\sigma) - F_3(2\chi)] \\
&\quad + \tfrac{1}{16}\cos\Delta\Phi_0\{4F_1(2\sigma) + 4F_1(\chi) \\
&\quad + F_1[2(\chi + \sigma)] + F_1[2(\chi - \sigma)] + F_3[2(\chi + \sigma)] \\
&\quad + F_3[2(\chi - \sigma)]\} - \tfrac{1}{8}\sin\Delta\Phi_0\{2F_2(\chi) \\
&\quad + F_2[2(\chi + \sigma)] + F_2[2(\chi - \sigma)]\}, \qquad (39)
\end{aligned}$$

respectively.

The relative intensities in the C2 and C3 detectors as functions of the tilt angle α are shown in Fig. 13 for both our symmetric and our skew-symmetric interferometers. The variation of interference fringe contrast as a function of α seen in this figure was first predicted by Bonse & Wroblewski (1983, 1984) using a spherical-wave approach. In this figure, the intensities are normalized to the sum intensity $\mathscr{I}_{C2}(\alpha) + \mathscr{I}_{C3}(\alpha)$ to account for the variations in the intensity due to the dependence on α of the real experimental distribution of neutron wavevectors accepted by the interferometer. We observe from equations (38) and (39) that the total intensity in the C2
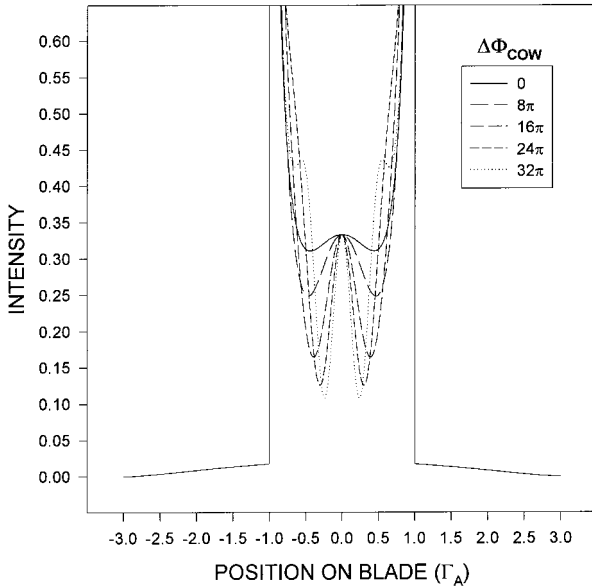

Fig. 9. Profile of the mean intensity across the C2 detector beam as predicted by dynamical diffraction at various values of $\Delta\Phi_{COW}$ for the symmetric interferometer.

and C3 detectors is not constant but instead dependent on tilt for an interferometer of the more general skew-symmetric geometry although it is constant for a symmetric interferometer. However, the amplitudes of the intensity oscillations in the two detectors due to the phase factor $\Delta\Phi_0$ are equal and opposite for the two interferometers.

A comparison of the predictions of this theory with experimental data measured using 1.8796 Å neutrons with the symmetric interferometer is shown in Fig. 14. Additional corrections to the theory (Littrell *et al.*, 1997) such as less than perfect fringe visibility when the interferometer is level and dephasing due to the distribution of angles of incidence for which the Bragg condition is satisfied have been included. There is very good qualitative agreement between the theory and the experimental data.

In our recent experiment (Littrell *et al.*, 1997), the gravitational phase shift was determined by subtracting the offset phase of an interferogram measured by varying the angle δ of the aluminium phase shifter with the interferometer level from the offset phase of one measured at tilt angle α. A series of phase-shifter scans illustrating the advance of the offset phase as the interferometer is tilted is shown in Fig. 15. After subtracting the calculated Sagnac phase shifts and
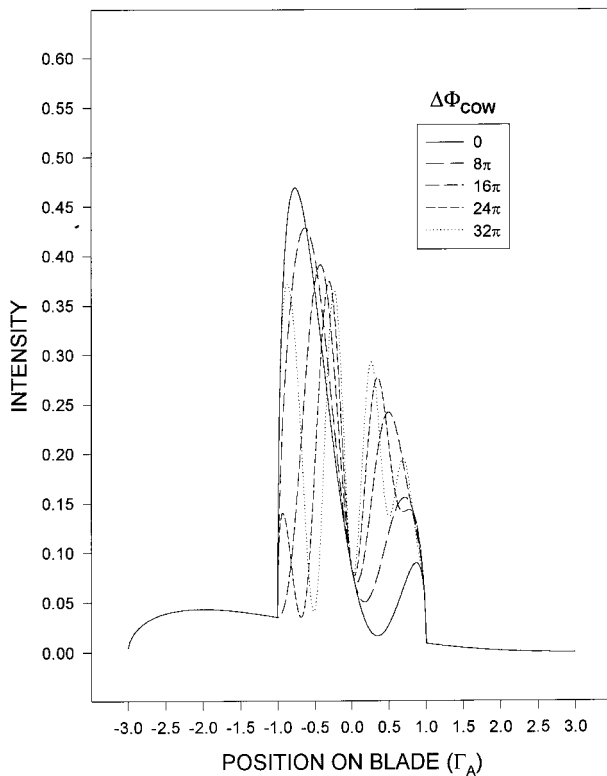
combining the data measured at both wavelengths used for each interferometer to remove the effects of bending, a discrepancy of the order of 1% between the measured phase shifts and those calculated from theory remains for both interferometers despite a statistical precision of the data of the order of 0.1%. Fig. 16 is a plot of the discrepancies between the theory and the data as a function of α. Since the measured phase shift is in between that predicted by the COW formula and that predicted including dynamical diffraction effects for all values of α except the large negative values near the limits of motion of the apparatus, the dynamical diffraction correction appears to be too large.

5. Single-beam internal interference effects

Earlier in this paper, we noted that the sum of the intensities in the C2 and C3 detectors are functions of the tilt angle α both in the total integrated intensity and in the intensity contribution for each value of Γ. This is surprising and somewhat disconcerting as it appears to be a violation of the idea of conservation of neutrons. The reason for this is clear upon closer examination of Fig. 5. Along beam I, the neutron trajectories labeled 6 and 7 recombine and interfere at the point on the mirror crystal exit surface labeled F_I. This interference results in a swapping of intensity between beam I and the beam leading to the C4 beam detector, Likewise, paths 2 and 3 recombine coherently at the point F_{II} to swap intensity back and forth between beam II and the side beam, *i.e.* the C1 detector beam. It is these interference loops and the similar ones in the back half of the interferometer

Fig. 10. Profile of the mean intensity across the C3 detector beam as predicted by dynamical diffraction at various values of $\Delta\Phi_{COW}$ for the symmetric interferometer.
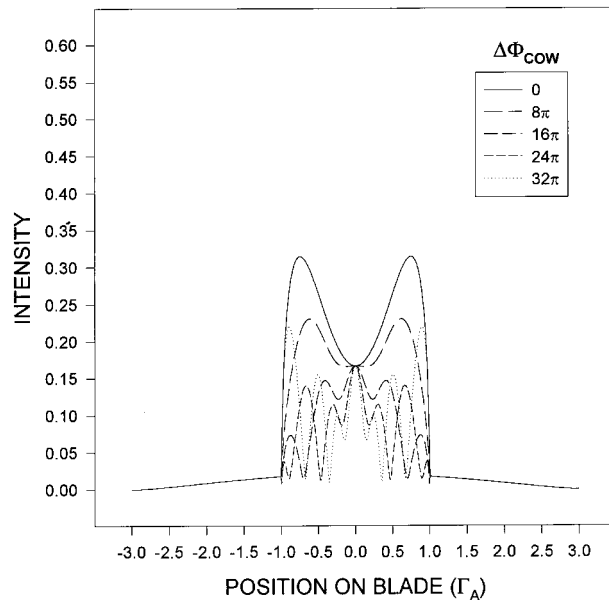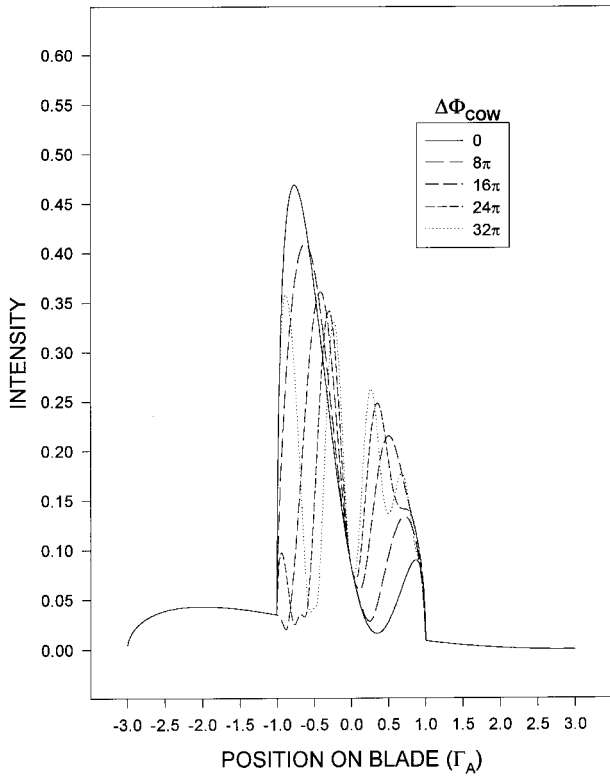

Fig. 11. Profile of the magnitude of intensity oscillations across the C2 detector beam as predicted by dynamical diffraction at various values of $\Delta\Phi_{COW}$ for the symmetric interferometer.

that give the primary-beam intensity profile its rich structure.

From the values of the phase accumulated along each path given in Tables 2 and 3, we find that the phase difference between paths 2 and 3 is given by

$$\Delta\Phi_2 - \Delta\Phi_3 = \Gamma(\chi - 2\sigma) \qquad (40)$$

and the phase difference between paths 6 and 7 by

$$\Delta\Phi_6 - \Delta\Phi_7 = \Gamma(\chi + 2\sigma). \qquad (41)$$

The phase shifts accumulated along paths 1, 4, 5 and 8 are not needed to calculate the intensities in the C1 and C4 beams and in beams I and II between the mirror and analyzer crystal blades. The amplitudes of the paths contributing intensity to the C1 beam and beam II after the mirror blade M_{II} are given in Tables 4 and 5, respectively. The amplitudes of the paths contributing intensity to beam I and the C4 beam after the mirror blade M_I are given in Tables 6 and 7. At the back surface to the mirror crystal M_{II} in beam II, the intensity as a function of incident Γ measured in the C1 detector is given by

$$I_{C1}(\alpha, \Gamma) = \tfrac{1}{4}(1 - \Gamma^2)^{-1/2}(1 + \Gamma^2) - \tfrac{1}{8}(1 - \Gamma^2)^{1/2}$$
$$\times \cos\Gamma(\chi - 2\sigma) \qquad (42)$$

Fig. 12. Profile of the magnitude of intensity oscillations across the C3 detector beam as predicted by dynamical diffraction at various values of $\Delta\Phi_{COW}$ for the symmetric interferometer.

and the intensity that continues along the interfering beam by

$$I_{II}(\alpha, \Gamma) = \tfrac{1}{8}(1 - \Gamma^2)^{1/2}[2 + \cos\Gamma(\chi - 2\sigma)]. \qquad (43)$$

Similarly, the intensities at the other mirror crystal M_I are

$$I_{C4}(\alpha, \Gamma) = \tfrac{1}{16}(1 - \Gamma^2)^{-3/2}[(1 + \Gamma)^4 + (1 - \Gamma)^4]$$
$$+ \tfrac{1}{8}(1 - \Gamma^2)^{1/2}[1 + \cos\Gamma(\chi + 2\sigma)] \qquad (44)$$

in the C4 beam, and

$$I_I(\alpha, \Gamma) = \tfrac{1}{4}(1 - \Gamma^2)^{-1/2}(1 + \Gamma^2)$$
$$- \tfrac{1}{8}(1 - \Gamma^2)^{1/2}\cos\Gamma(\chi + 2\sigma) \qquad (45)$$

along beam I. The reason why the sum intensity in the C2 and C3 detectors is not constant is now evident. We see from equation (43) that paths 2 and 3 interfere constructively in the interfering beam when the interferometer is level so that the total intensity in beam II is increased. Likewise, equation (45) shows that paths 6 and 7 interfere destructively so that the intensity in beam I is reduced. However, the tilt-angle-dependent phase shift along beam I oscillates faster than the phase shift in beam II when $d_2 > d_1$ (as shown in Fig. 5).
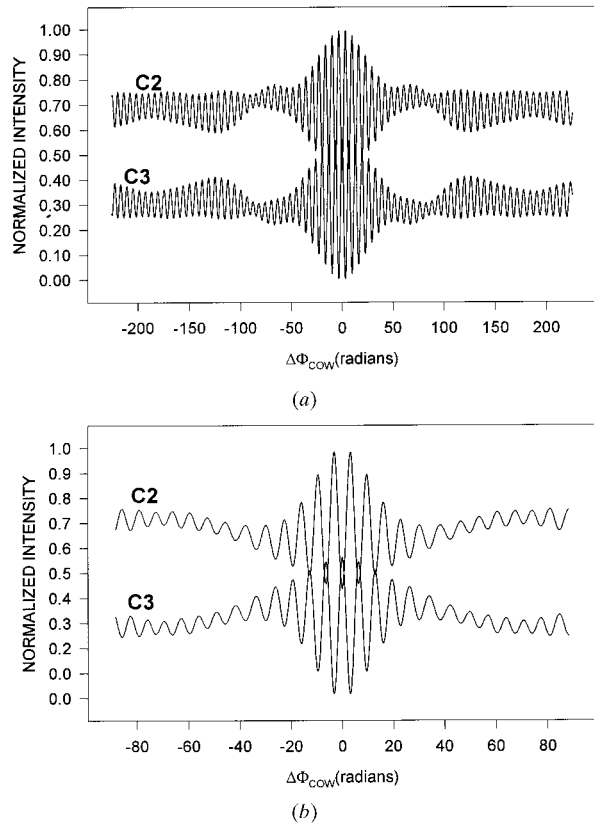

Fig. 13. Theoretically predicted tilt-angle interferograms normalized to C2+C3 to compensate for the dependence on tilt of the intensity of neutrons accepted by the interferometer: (a) the symmetric interferometer; (b) the skew-symmetric interferometer.

Table 4. *Amplitudes of the paths in the C1 detector or side beam*

Path	Coefficient	Amplitude
1	$R_\alpha(\Gamma)T_\alpha(-\Gamma)$	$\frac{1}{4}(1-\Gamma^2)^{1/2}(1+\Gamma)$
2	$R_\alpha(\Gamma)T_\beta(-\Gamma)$	$\frac{1}{4}(1-\Gamma^2)^{1/2}(1-\Gamma)$
3	$R_\beta(\Gamma)T_\alpha(-\Gamma)$	$-\frac{1}{4}(1-\Gamma^2)^{1/2}(1+\Gamma)$
4	$R_\beta(\Gamma)T_\beta(-\Gamma)$	$-\frac{1}{4}(1-\Gamma^2)^{1/2}(1-\Gamma)$

Table 5. *Amplitudes of the paths in beam II between the intermediate or mirror blade and the analyzer blade of the interferometer*

Path	Coefficient	Amplitude
1	$R_\alpha(\Gamma)R_\alpha(-\Gamma)$	$\frac{1}{4}(1-\Gamma^2)$
2	$R_\alpha(\Gamma)R_\beta(-\Gamma)$	$-\frac{1}{4}(1-\Gamma^2)$
3	$R_\beta(\Gamma)R_\alpha(-\Gamma)$	$-\frac{1}{4}(1-\Gamma^2)$
4	$R_\beta(\Gamma)R_\beta(-\Gamma)$	$\frac{1}{4}(1-\Gamma^2)$

One of the consequences of the tilt-dependent variation of the intensity between the mirror and analyzer blades of the interferometer is that the intensity measured in the C2 and C3 detectors will vary even if beam I or beam II is blocked. For example, if beam I is blocked, then the intensity of distributions as a function of incident Γ are given by

$$I_{\mathrm{IIC2}}(\alpha, \Gamma) = \tfrac{1}{16}(1-\Gamma^2)^{3/2}[2 + \cos 2\Gamma\chi + \cos \Gamma(\chi + 2\sigma)$$
$$+ \cos \Gamma(\chi - 2\sigma)] \qquad (46)$$

for the C2 detector, and

$$I_{\mathrm{IIC3}}(\alpha, \Gamma) = \tfrac{1}{16}(1-\Gamma^2)^{1/2}(1+\Gamma^2)[2 + \cos \Gamma(\chi - 2\sigma)]$$
$$- \tfrac{1}{16}(1-\Gamma^2)^{3/2}[\cos 2\Gamma\chi + \cos \Gamma(\chi + 2\sigma)] \qquad (47)$$

for the C3 detector. Likewise, the intensity distributions in the C2 and C3 detector beams when beam II is blocked are given by

$$I_{\mathrm{IC2}}(\alpha, \Gamma) = \tfrac{1}{32}(1-\Gamma^2)^{-1/2}[(1+\Gamma)^4 + (1-\Gamma)^4$$
$$+ 2(1-\Gamma^2)^2(1 + \cos 2\Gamma\chi)]$$
$$- \tfrac{1}{16}(1-\Gamma^2)^{1/2}(1+\Gamma^2)[\cos \Gamma(\chi - 2\sigma)$$
$$+ \cos \Gamma(\chi + 2\sigma)] \qquad (48)$$

and

$$I_{\mathrm{IC3}}(\alpha, \Gamma) = \tfrac{1}{16}(1-\Gamma^2)^{1/2}(1+\Gamma^2)[2 + \cos \Gamma(\chi - 2\sigma)]$$
$$- \tfrac{1}{16}(1-\Gamma^2)^{3/2}[\cos 2\Gamma\chi + \cos \Gamma(\chi + 2\sigma)]. \qquad (49)$$

These single-beam intensity distributions, like those including contributions from both beams, are even functions of G. The tilt-dependent mean values of the
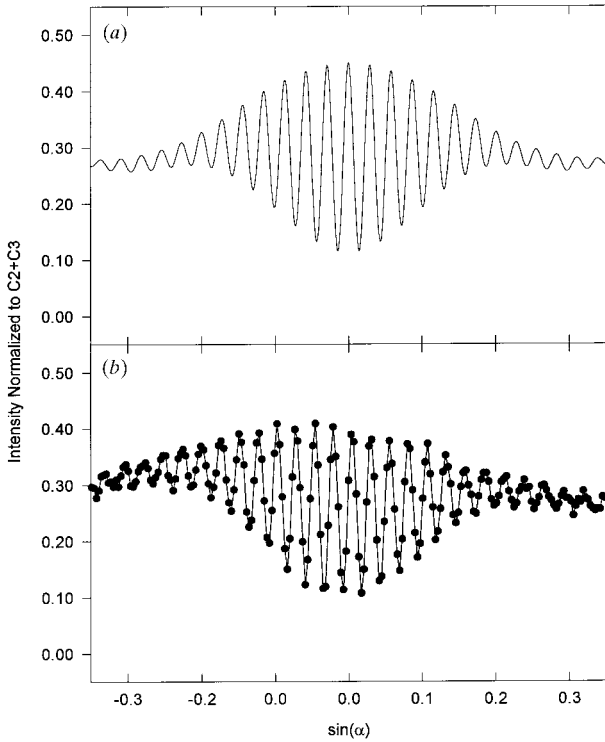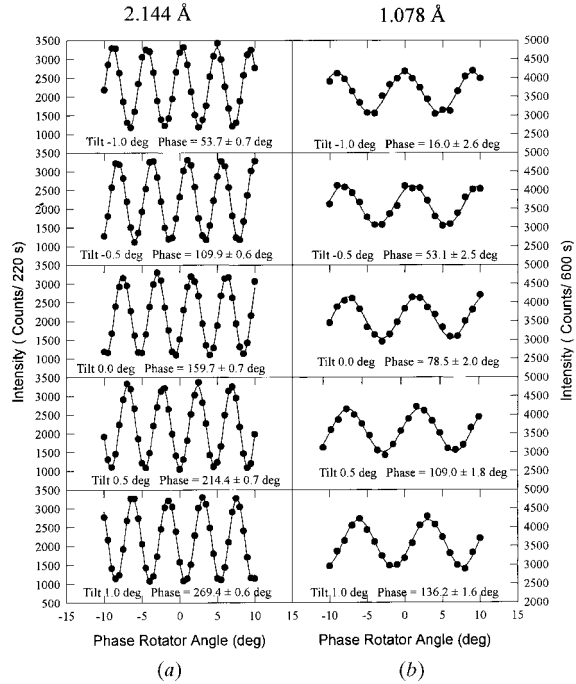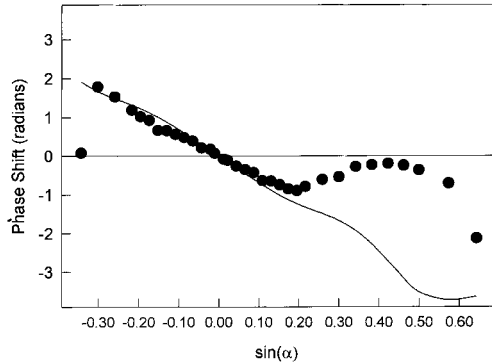

Fig. 14. Comparison of the theoretically predicted normalized tilt-angle interferogram scaled to match visibility at $\alpha = 0°$ with experimentally observed data for 1.8796 Å neutrons in the symmetric interferometer. (*a*) Theoretical prediction. (*b*) Experimental data.

Fig. 15. A series of phase rotator scans taken for various values of *a* using the wavelengths (*a*) 2.1440 Å and (*b*) 1.0780 Å in the skew-symmetric interferometer. The phase advances almost the same amount with each step and nearly twice as much for the 2.1440 Å data as for the 1.0780 Å data.

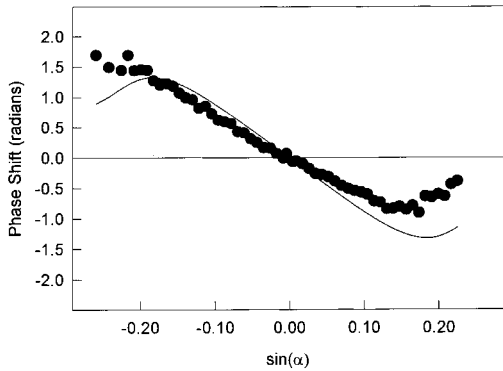Table 6. *Amplitudes of the paths in the C4 detector or monitor beam*

Path	Coefficient	Amplitude
5	$T_\alpha(\Gamma)T_\alpha(\Gamma)$	$\frac{1}{4}(1-\Gamma^2)$
6	$T_\alpha(\Gamma)T_\beta(\Gamma)$	$\frac{1}{4}(1-\Gamma^2)$
7	$T_\beta(\Gamma)T_\alpha(\Gamma)$	$\frac{1}{4}(1-\Gamma^2)$
8	$T_\beta(\Gamma)T_\beta(-\Gamma)$	$\frac{1}{4}(1+\Gamma^2)$

Table 7. *Amplitudes of the paths in beam I between the intermediate or mirror blade and the analyzer blade of the interferometer*

Path	Coefficient	Amplitude
5	$T_\alpha(\Gamma)R_\alpha(\Gamma)$	$\frac{1}{4}(1-\Gamma^2)^{1/2}(1-\Gamma)$
6	$T_\alpha(\Gamma)R_\beta(\Gamma)$	$-\frac{1}{4}(1-\Gamma^2)^{1/2}(1-\Gamma)$
7	$T_\beta(\Gamma)R_\alpha(\Gamma)$	$\frac{1}{4}(1-\Gamma^2)^{1/2}(1+\Gamma)$
8	$T_\beta(\Gamma)R_\beta(\Gamma)$	$-\frac{1}{4}(1-\Gamma^2)^{1/2}(1+\Gamma)$

intensity distributions in the C2 and C3 detector beams given in equations (25) and (26) are the sums of the contributions to the distributions from the two beams.

While the area enclosed between the paths is different for each value of Γ, the points F_I and F_II are fixed at the position $\Gamma_M = 0$. Since there is a focused image of the incident beam at these points, the portions of beam I and beam II in the back half of the interferometer coming from points F_I and F_II are referred to as the focused beams. Likewise, we refer to the beams coming from points A and C at position $\Gamma_M = 2\Gamma$ and B and D at $\Gamma_M = -2\Gamma$ as the defocused beams. Thus, the distribu-

tion of neutrons exiting the mirror blade at position D as a function of Γ_M is

$$P_D(\Gamma_M) = \tfrac{1}{2}[1-(\Gamma_M/2)^2]^{-3/2} \qquad (50)$$

based on the assumed distributions in y and Γ of the incident beam given by equations (23) and (24), respectively. Neutrons with a given value of Γ contribute an intensity of

$$I_{C1D}(\alpha, \Gamma) = \tfrac{1}{8}(1-\Gamma^2)^{-1/2}(1+\Gamma^2) \qquad (51)$$

to the defocused beam and

$$\begin{aligned} I_{C1F}(\alpha, \Gamma) = &\tfrac{1}{8}(1-\Gamma^2)^{-1/2}(1+\Gamma^2) \\ &-\tfrac{1}{8}(1-\Gamma^2)^{1/2}\cos\Gamma(\chi-2\sigma) \end{aligned} \qquad (52)$$

to the focused beam to the C1 detector, and intensities of

$$I_{IID}(\alpha, \Gamma) = \tfrac{1}{8}(1-\Gamma^2)^{1/2} \qquad (53)$$

to the defocused beam and

$$I_{IIF}(\alpha, \Gamma) = \tfrac{1}{8}(1-\Gamma^2)^{1/2}[1+\cos\Gamma(\chi-2\sigma)] \qquad (54)$$

to the focused beam continuing along beam II. The intensity profiles at the exit surface of the mirror blade are thus

$$\begin{aligned} I_{C1}(\alpha, \Gamma_M) = &\tfrac{1}{16}[1-(\Gamma_M/2)^2]^{1/2}(1+\Gamma_M/2)^2 \\ &+\tfrac{1}{8}\delta(\Gamma_M)\int_{-1}^{1}[(1-\Gamma^2)^{-1/2}(1+\Gamma^2) \\ &-(1-\Gamma^2)^{1/2}\cos\Gamma(\chi-2\sigma)]\,d\Gamma \end{aligned} \qquad (55)$$

for the C1 detector, and

$$\begin{aligned} I_{II}(\alpha, \Gamma_M) = &\tfrac{1}{16}[1-(\Gamma_M/2)^2]^{1/2}+\tfrac{1}{8}\delta(\Gamma_M) \\ &\times \int_{-1}^{1}\{(1-\Gamma^2)^{1/2}[1+\cos\Gamma(\chi-2\sigma)]\}\,d\Gamma \end{aligned}$$

$$(56)$$

continuing in beam II, where $\delta(\Gamma_M)$ is the Dirac δ function at $\Gamma_M = 0$. Following a similar analysis, the intensity profiles in the C4 detector beam and along beam I are given by

Fig. 16. Graphical representation of the difference between the phase shift measured using (a) the skew-symmetric interferometer and (b) the symmetric interferometer and $\Delta\Phi_{COW}$. The solid curves are the difference between the theoretical gravitational phase shift and $\Delta\Phi_{COW}$.

$$I_{C4}(\alpha, \Gamma_M) = \tfrac{1}{32}[1 - (\Gamma_M/2)^2]^{-3/2}[(1 + \Gamma_M/2)^4$$
$$+ (1 - \Gamma_M/2)^4] + \tfrac{1}{8}\delta(\Gamma_M)$$
$$\times \int_{-1}^{1} \{(1 - \Gamma^2)^{1/2}[1 + \cos\Gamma(\chi + 2\sigma)]\}\,d\Gamma$$

$$(57)$$

and

$$I_{I}(\alpha, \Gamma_M) = \tfrac{1}{16}[1 - (\Gamma_M/2)^2]^{-1/2}(1 - \Gamma_M/2)^2 + \tfrac{1}{8}\delta(\Gamma_M)$$
$$\times \int_{-1}^{1} [(1 - \Gamma^2)^{-1/2}(1 + \Gamma^2) - (1 - \Gamma^2)^{1/2}$$
$$\times \cos\Gamma(\chi + 2\sigma)]\,d\Gamma, \qquad (58)$$

respectively. These intensity profiles are shown in Fig. 17.

These intensity distributions lead to a total intensity measured in the C1 detector of

$$\mathscr{I}_{C1}(\alpha) = \int_{-1}^{1} I_{C1}(\alpha, \Gamma)\,d\Gamma = (3\pi/8) - \tfrac{1}{8}F_3(\chi - 2\sigma). \quad (59)$$

If beam I is blocked, the total intensities in the C2 and C3 detector beams become

$$\mathscr{I}_{IIC2}(\alpha) = (3\pi/64) - \tfrac{1}{16}[F_1(\chi + 2\sigma) + F_1(\chi - 2\sigma)$$
$$+ F_1(2\chi)] + \tfrac{1}{16}[F_3(\chi + 2\sigma) + F_3(\chi - 2\sigma)$$
$$+ F_3(2\chi)] \qquad (60)$$

and

$$\mathscr{I}_{IIC3}(\alpha) = (5\pi/64) + \tfrac{1}{16}[F_1(\chi + 2\sigma) + F_1(\chi - 2\sigma)$$
$$+ F_1(2\chi)] - \tfrac{1}{16}[F_3(\chi + 2\sigma) - F_3(\chi - 2\sigma)$$
$$+ F_3(2\chi)]. \qquad (61)$$

In this situation, the intensities in the C1, C2, and C3 detectors sum to $\pi/2$ These predictions are compared with experimental results in Fig. 18. As before, both the theoretical curves and the data have been normalized to the total intensity to account for any α-dependent variation in the intensity accepted by the interferometer. The theory appears to overestimate the rate at which the measured intensity varies due to gravitational phase shifts in single path interference in a manner similar to that noted previously in COW experiments where the dynamical diffraction effects were considered (Werner *et al.*, 1988; Littrell *et al.*, 1997). If beam II is blocked, then the intensities measured by the C2 and C3 detectors are

$$\mathscr{I}_{IC2}(\alpha) = (19\pi/64) - \tfrac{1}{16}[F_1(\chi + 2\sigma) + F_1(\chi - 2\sigma)$$
$$+ F_1(2\chi)] - \tfrac{1}{16}[F_3(\chi + 2\sigma) + F_3(\chi - 2\sigma)$$
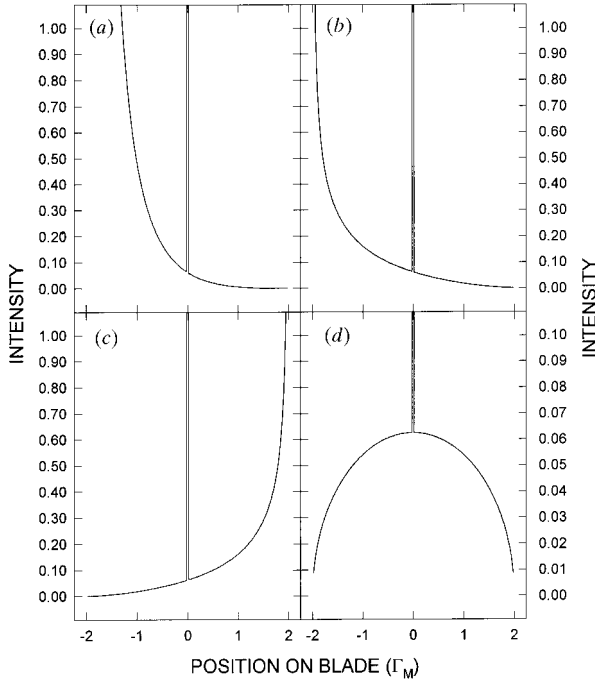$$- F_3(2\chi)] \qquad (62)$$

Fig. 17. Intensity profiles of (*a*) the C4 or monitor detector beam, (*b*) beam I, (*c*) the C1 detector or side beam and (*d*) beam II after the intermediate or mirror blades of the interferometer at tilt angle $\alpha = 0°$.
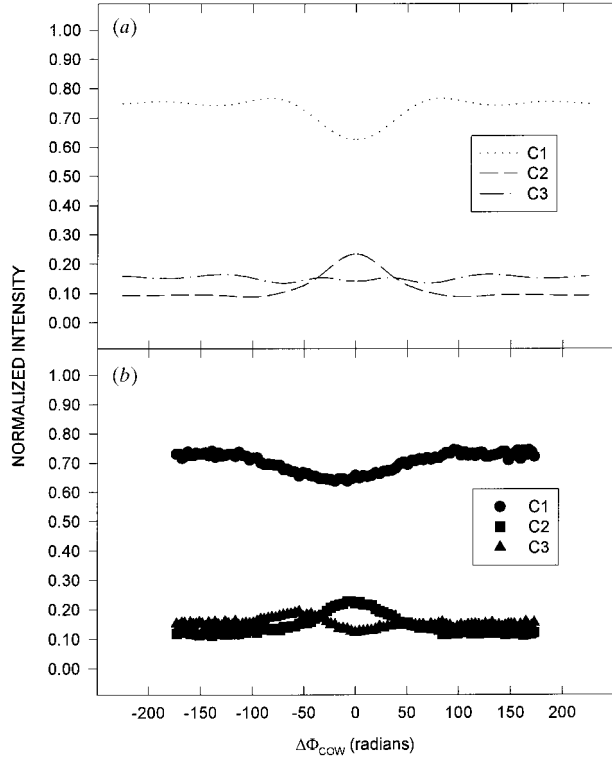

Fig. 18. Comparison of (*a*) the theoretically predicted normalized tilt-angle interferogram measured with beam I blocked by an absorber (normalized to the sum of the intensities in the C1, C2 and C3 detectors) with (*b*) experimentally observed data for 1.8796 Å neutrons in the symmetric interferometer.

and

$$\mathscr{I}_{\mathrm{IC3}}(\alpha) = (5\pi/64) + \tfrac{1}{16}[F_1(\chi + 2\sigma) + F_1(\chi - 2\sigma)$$
$$+ F_1(2\chi)] - \tfrac{1}{16}[F_3(\chi + 2\sigma) - F_3(\chi - 2\sigma)$$
$$+ F_3(2\chi)]. \tag{63}$$

A comparison of experimental data with the predicted intensity in the C2 and C3 detectors normalized to their sum is shown in Fig. 19. Since the total intensity of the defocused-beam contribution to the C4 detector as predicted by this theory is infinite, just like the total incident intensity, the prediction for the total intensity in the C4 detector is meaningless. However, the total intensity in the focused beam to the C4 detector is finite and given by

$$\mathscr{I}_{\mathrm{C4F}} = \tfrac{1}{8} \int\limits_{-1}^{1} \{(1 - \Gamma^2)^{1/2}[1 + \cos\Gamma(\chi + 2\sigma)]\}\, d\Gamma$$
$$= \pi/16 + \tfrac{1}{8}F_3(\chi + 2\sigma). \tag{64}$$

The sum of the intensities in the C2 and C3 beams and the focused portion of the C4 beam is independent of α when beam II is blocked. Although the sum of the intensities in C2 and C3 is α-dependent, the sum of the intensities in all four detectors is independent of tilt.
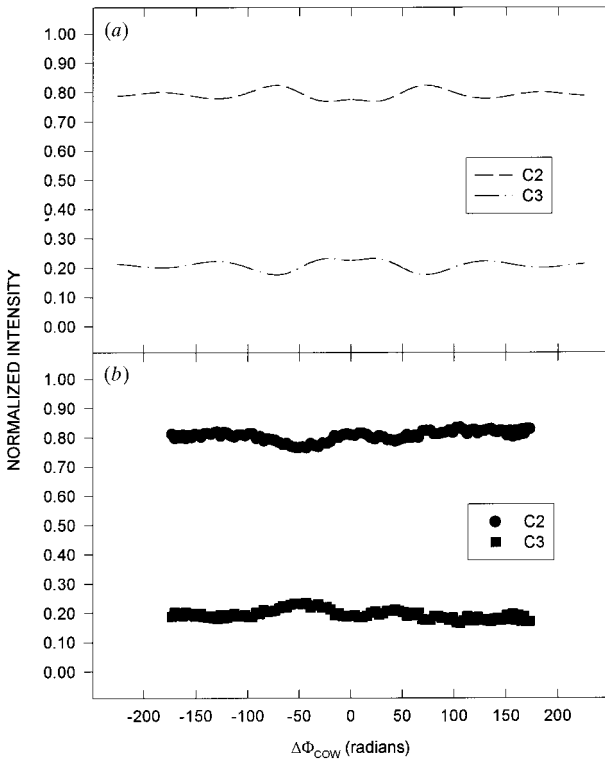

Fig. 19. Comparison of (a) the theoretically predicted normalized tilt-angle interferogram measured with beam I blocked by an absorber (normalized to the sum of the intensities in the C2 and C3 detectors) with (b) experimentally observed data for 1.8796 Å neutrons in the symmetric interferometer.

Thus, the principle of conservation of neutrons is satisfied.

6. Interferometry with restricted beams

In certain situations in neutron interferometry experiments, it is advantageous to restrict the size or profile of the neutron beams within the interferometer. One example of such a situation is an experiment involving a small or inhomogeneous sample. In order to properly interrogate the sample, a narrow neutron beam is needed. A natural way of achieving this condition is suggested by the existence of the focused beams after the mirror blades. By using a narrow incident slit and identical slits on the back surface of one or both of the mirror blades, the spreading of the beam due to diffraction can in principle be overcome to make a narrow coherent beam. The mean intensities and amplitudes of oscillation predicted for the C2 and C3 detectors for various combinations of focused, defocused and unrestricted beams with the interferometer level are given in Table 8. From this table, we observe that a narrow beam is best obtained by using the focused part of beam II and all of beam I. If the focused part of both beams is used, interference is quite poor as the distribution in Γ is quite different for the two beams and each Γ component interferes only with itself.

7. Conclusions

The apparently simple Mach–Zehnder geometry of the neutron interferometer is actually quite complex. The splitting of the incident beam into multiple currents forming multiple interferometric loops by dynamical diffraction processes leads to subtle effects in COW-type gravity experiments. Although inclusion of these effects greatly enhances the agreement between theory and experiment both qualitatively and quantitatively, significant discrepancies remain. One problem is that the magnitudes of observed phase shifts due to gravity are consistently lower than theoretically predicted. Another difficulty is that the tilt-angle interferograms are always asymmetric between positive and negative tilts, even though theory predicts symmetric interferograms.

One possible source of these difficulties is a coupling between bending and strain in the interferometer crystals and the dynamical diffraction corrections. Our previous assumption that bending and strain are decoupled from dynamical diffraction is likely to be incorrect. As seen from equation (14), the off-Bragg parameter y depends on both the magnitude and sign of Γ. Any strains or bending of the crystal will necessarily change either the lattice spacing of the interferometer blades or the orientation of the lattice planes of the blades relative to one another. Thus, y may be slightly different for each blade, contrary to the assumption used in carrying out these calculations that y (and, more

Table 8. *Mean intensities and amplitudes of oscillation in the C2 and C3 detector beams at α = 0° for various combinations of the focused and defocused beams*

Beam I	Beam II	C2 mean	C2 amplitude	C3 mean	C3 amplitude
Focused	Focused	$5\pi/32$	$-\pi/32$	$3\pi/32$	$\pi/32$
Focused	Defocused	$17\pi/128$	$-\pi/64$	$7\pi/128$	$\pi/64$
Focused	Open	$29\pi/128$	$-3\pi/64$	$11\pi/128$	$3\pi/64$
Defocused	Focused	$17\pi/128$	$-5\pi/64$	$11\pi/128$	$5\pi/64$
Defocused	Defocused	$11\pi/64$	$-\pi/64$	$5\pi/64$	$\pi/64$
Defocused	Open	$5\pi/32$	$-3\pi/32$	$\pi/8$	$3\pi/32$
Open	Focused	$37\pi/128$	$-3\pi/64$	$19\pi/128$	$7\pi/84$
Open	Defocused	$19\pi/64$	$-\pi/32$	$7\pi/64$	$\pi/32$
Open	Open	$23\pi/64$	$-9\pi/64$	$9\pi/64$	$9\pi/64$

importantly, Γ) is the same in all blades. Two methods have been suggested for avoiding these difficulties. Either the experiment can be performed with the interferometer submerged in a neutron-transparent fluid that has the same density as silicon (see comments in Werner *et al.*, 1988; Werner, 1997) or the interferometer can be rotated about an axis of symmetry (Littrell *et al.*, 1997). Although these techniques may reduce or even remove any dependence of the bending of the interferometer on the tilt angle, they do nothing to solve the problem of static residual strains inevitably produced in the process of manufacturing and mounting the interferometer.

Another possible source of discrepancy is the assumption of a narrow entrance slit. The analysis presented here is valid if the entrance slit width is much smaller than the interferometer blade thickness. In the actual experimental apparatus, we used circular apertures with diameters of more than twice the thickness of the interferometer blades. For this situation, it may be equally valid to consider the effects of a narrow slit on the exit face of the first or splitter crystal. The natural way to resolve doubts relating to this difficulty is to repeat the experiment with a narrow entrance slit and perhaps again with a large entrance slit and a narrow slit on the back surface of the splitter blade, using position-sensitive detectors in the exit beams to include information about the distribution of neutrons across the beams as well as the integrated intensity. In such a study of the transverse intensity distribution (and phase-shift distribution in the **0** and **G** beams), it is necessary to use entrance slits that are narrow in the scattering plane of the interferometer and high-resolution position-sensitive detectors to prevent averaging of the fine structure expected to be present rendering it undetectable. However, these methods do nothing to resolve the problems associated with bending and strain, although they may provide a way to study them through Moiré fringes.

It may be that the best way to decouple the dynamical diffraction effects from those due to bending and strain is to use a restricted beam geometry. One way to do this [the method used to separate the beams in two-crystal interferometers (Zeilinger *et al.*, 1979)] is to use narrow slits on both the entrance and exit sides of the splitter crystal so that only a small range of Γ is accepted by the interferometer. Another approach would be to use a symmetric interferometer and mask the C2 and C3 detector beams so that the primary paths are excluded. According to equations (30) and (32), the contribution to the dynamical diffraction phase shift from the maverick paths is entirely due to the asymmetry of the interferometer. The difficulty with either of these approaches is that the neutron counting rates would be greatly reduced, both increasing the length of time needed to complete the experiment and decreasing the signal-to-noise ratio of the data.

A further possible source of discrepancy is the perturbative nature of this theoretical calculation. Dynamical diffraction within a single crystal is highly dispersive in the sense that neutrons with only slightly different wavevector can differ tremendously in their trajectories through the crystal. As Werner (1980) has shown theoretically and Raum *et al.* (1995, 1997) have demonstrated experimentally, this leads to an enhancement of the curvature due to gravity of the trajectories of neutrons within the crystal. However, numerical simulations including this effect by Werner *et al.* (1988) show that this leads to an increase in magnitude of the dynamical diffraction correction phase. This change is both too small to account for the discrepancy between the theory and the experimental data and in the wrong direction. Bonse & Wroblewski (1983, 1984) have performed a similar calculation to describe the dynamical diffraction effects in an accelerating interferometer.

Finally, we would like to say a word about dynamical diffraction effects due to other potentials. These diffraction corrections are not unique to the effects of gravity. Since the phase difference between any two of the paths predicted by dynamical diffraction is proportional to the area between them, the Sagnac phase shift will necessarily require similar corrections. These corrections can be simply obtained by substituting $\Delta\Phi_{\text{Sagnac}}$ for $\Delta\Phi_{\text{COW}}$ in all of the equations. Likewise, if the interferometer is in a magnetic field gradient, then calculation of the phase shift due to the Zeeman potential $V(\mathbf{r}) = \boldsymbol{\mu}_n \cdot \mathbf{B}(\mathbf{r})$ will also require knowledge of

dynamical diffraction corrections. The functional form for the dynamical diffraction correction for the phase shift due to a magnetic field gradient will be essentially the same if the gradient is constant in position but substantially different otherwise.

References

Anandan, J. (1979). *Phys. Rev. D*, **15**, 1448–1464.

Anandan, J. (1981). *Phys. Rev. D*, **24**, 338–350.

Atwood, D. K., Horne, M. A., Shull, C. G. & Arthur, J. A. (1984). *Phys. Rev Lett.* **52**, 1673–1676.

Bonse, U. & Hart, M. (1965). *Appl. Phys. Lett.* **6**, 155–156.

Bonse, U. & Wroblewski, T. (1983). *Phys. Rev. Lett.* **51**, 1401–1404.

Bonse, U. & Wroblewski, T. (1984). *Phys. Rev. D*, **30**, 1214–1224.

Colella, R., Overhauser, A. W. & Werner, S. A. (1975). *Phys. Rev. Lett.* **34**, 1472–1474.

Dirac, P. A. M. (1945). *Rev. Mod. Phys.* **17**, 195–199.

Feynman, R. P. (1948). *Rev. Mod. Phys.* **20**, 367–387.

Greenberger, D. M. & Overhauser, A. W. (1979). *Rev. Mod. Phys.* **51**, 43–63.

Horne, M. A. (1986). *Physica (Utrecht)*, B**137**, 260–265.

Jacobson, D. L. (1997). Doctoral dissertation, University of Missouri–Columbia, USA. Unpublished.

Koester, L. (1975). *Phys. Rev. D*, **14**, 907–909.

Littrell, K., Allman, B., Hoag, K. & Werner, S. A. (1996). *J. Phys. Soc. Jpn*, A**65**, 86–88.

Littrell, K., Allman, B. & Werner, S. A. (1997). *Phys. Rev. A*, **56**, 1767–1780.

Opat, G. I. (1995). *Advances in Quantum Phenomena*, edited by E. G. Beltrometti, pp. 89–94. New York: Plenum Press.

Page, L. A. (1975). *Phys. Rev. Lett.* **35**, 543–544.

Petrascheck, D. (1979). *Neutron Interferometry*, edited by U. Bonse & H. Rauch, pp. 108–132. Oxford/New York: Clarendon Press.

Petrascheck, D. & Folk, R. (1976). *Phys. Status Solidi A*, **36**, 147–160.

Rauch, H., Treimer, W. & Bonse, U. (1974). *Phys. Lett.* A**47**, 369–372.

Rauch, H., Wölwitsch, H., Kaiser, H., Clothier, R. & Werner, S. A. (1996). *Phys. Rev. A*, **53**, 902–908.

Raum, R., Koellner, M., Zeilinger, A., Arif, M. & Gähler, R. (1995). *Phys. Rev. Lett.* **74**, 2859–2862.

Raum, R., Weber, M., Gähler, R. & Zeilinger, A. (1997). *J. Phys. Soc. Jpn*, A**65**, 277–279.

Roll, P., Krotov, G. R. & Dicke, R. H. (1967). *Ann. Phys. (NY)*, **26**, 442.

Sagnac, M. G. (1913a). *CR Acad. Sci. (Paris)*, **157**, 708.

Sagnac, M. G. (1913b). *CR Acad. Sci. (Paris)*, **157**, 1410.

Shull, C. G., Zeilinger, A., Squires, G. L., Horne, M. A., Atwood, D. K. & Arthur, J. (1980). *Phys. Rev. Lett.* **44**, 1715–1718.

Staudenmann, J.-L., Werner, S. A., Colella, R. & Overhauser, A. W. (1980). *Phys. Rev. A*, **21**, 1419–1438.

Stodolsky, L. (1979). *Neutron Interferometry*, edited by U. Bonse & H. Rauch, pp. 313–328. Oxford/New York: Clarendon Press.

Werner, S. A. (1980). *Phys. Rev. B*, **21**, 1774–1789.

Werner, S. A. (1994). *Class. Quantum Grav.* **11**, A207–A226.

Werner, S. A. (1996). *J. Phys. Soc. Jpn*, **65**, Suppl. A, 51–59.

Werner, S. A., Kaiser, H., Arif, M. & Clothier, R. (1988). *Physica (Utrecht)*, B**151**, 22–35.

Werner, S. A., Kaiser, H., Arif, M., Hu, H.-C. & Berliner, R. (1986). *Physica (Utrecht)*, **136**, 137–140.

Werner, S. A., Staudenmann, J.-L. & Colella, R. (1979). *Phys Rev. Lett.* **42**, 1103–1106.

Zeilinger, A., Shull, C. G., Horne, M. A. & Squires, G. L. (1979). *Neutron Interferometry*, edited by U. Bonse & H. Rauch, pp. 48–59. Oxford/New York: Clarendon Press.